Micromechanics of the large-deformation response of semi-crystalline polymers

Algera, R.

Award date:
2020

Technische Universiteit
Eindhoven
University of Technology

De Rondom 70, 5612 AP Eindhoven
P.O. Box 513, 5600 MB Eindhoven
The Netherlands
www.tue.nl

Micromechanics of the large-deformation response of semi-crystalline polymers

Mechanics of Materials
Master graduation project

Academic year 2019, Jun. 10 till Feb. 4

Supervisors: Dr. Ir. J.A.W. van Dommelen
H.N. Chávez Thielemann

Student: R. Algera
Studentnumber: 0891726

Abstract

Semi-crystalline polymers are used in numerous products due to their advantageous characteristics. However, the material behaviour of the product is highly dependent on the processing conditions. To be able to predict the material response, the influence of these conditions needs to be modelled. Since the semi-crystalline polymer consists of two phases, the amorphous phase and the crystalline phase, these need to be modelled separately. This is done using a micro-mechanical model called the Composite Inclusion model (CIM). The CIM is a elasto-viscoplastic model, with the amorphous phase modelled by the EGP model, and the crystalline phase by a crystal plasticity model.
Some semi-crystalline materials, under certain processing conditions, show voiding in the amorphous phase during tensile loading. This has a large effect on the material response after yield. To be able to model this effect, a Gurson model was incorporated in the EGP model. In this study the implementation is explained and the effects on the material response for α i-PP are discussed. This is done by both looking at a pure EGP model and the CIM. These results are compared to present experimental results.
The purely EGP model seems to be able to predict the right trends, while for the CIM some problems were encountered. These problems seem to originate from a single inclusion, which shows large strain, resulting in enormous voiding in this inclusion. A look at this problem was provided to be able to resolve this problem for the complete CIM model.

List of Symbols

Symbol	Definition	Unit
$\vec{n}$	Interface normal	[]
$\vec{c}$	Chain direction	[]
$G_{i,j}$	Shear modulus	GPa
G_r	Hardening shear modulus	GPa
$\eta_{i,j}$	Viscosity	Pa· s
τ	Equivalent stress	MPa
D	Deformation rate	s^{-1}
$\boldsymbol{\sigma}_s$	Driving stress	MPa
κ	Bulk modulus	MPa
J	Volumetric change, det(F)	[]
B	Left Cauchy Green strain tensor	[]
μ	Pressure dependancy parameter	[]
P	Pressure	MPa
S_i	Aging parameter	[]
F	Deformation gradient	[]
L	Velocity tensor	s^{-1}
$\dot{\gamma}$	Equivalent shear rate	s^{-1}
$\vec{s}_0$	Unit slip direction	[]
$\vec{n}_0$	Unit slip plane normal	[]
ΔU	Activation energy of slip system	kJ/mol
V_{act}	Activation volume of slip system	[]
f	Void volume fraction	[]
Φ	Gurson potential	[]
C	Right Cauchy Green strain tensor	[]
s	standard deviation	[]

Notation

Symbol	Definition
$\dot{.}^h$	Hydrostatic part
$\dot{.}^d$	Deviatoric part
$\dot{.}_p$	Plastic part
$\dot{.}_e$	Elastic part
$\tilde{\dot{.}}$	Isochoric part
$\dot{.}_{i,j}$	Phase i, mode j
$\dot{.}^a$	Amorphous phase
$\dot{.}^c$	Crystal phase

Contents

1 Introduction

Semi-Crystalline polymers are used in numerous products due to their advantageous characteristics. These include low weight, low cost, they can be easily processed and they show good strength at high temperatures. These advantages allow for use in a wide range of products, including load-bearing products. However, for these polymers, the processing conditions have a large influence on the material response. These materials may be subjected to plastic deformations during processing. This causes orientation of molecular chains, resulting in different mechanical behaviour. As these polymers are widely used, it is important to be able to predict the resulting material response.
To understand these influences and simulate the polymer, to be able to predict the material characteristics, a model has been made. The base for the current model was first developed by Lee et al [1]. It featured a two phase model, as a semi-crystalline polymer consists of an amorphous phase and a crystalline phase. This work was expanded to incorporate elasto-viscoplastic properties by van Dommelen et al [2]. To account for the anisotropic characteristics in the amorphous phase Poluektov et al. [3] implemented the EGP model, first proposed by Tervoort et al. [4], in the elasto-viscoplastic model. This model is currently being fitted to i-PP characteristics. i-PP shows a large dependence on phase composition, α, β or γ, and temperature. During deformation of semi-crystalline materials voiding may also take place, as seen in Figure 1.1. Voiding shows in the amorphous phase and has a large influence on the material response. The amount of voids seems very dependent on the testing conditions [7]. First, an explanation is given about the origin of this phenomenon in Section 2. Then, in Section 3 a way to incorporate this into a elasto-viscoplastic framework is shown. This resulting model is called the Composite Inclusion Model, or CIM.

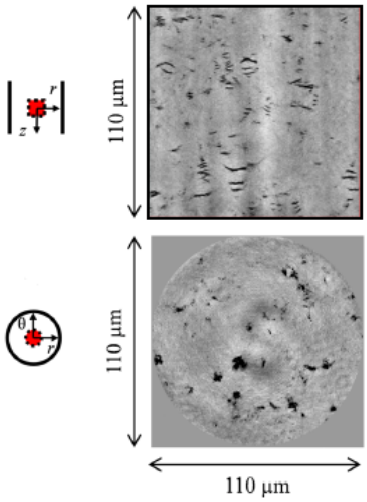

Figure 1.1: *Voiding of polyamide 6 under tension. [5]*

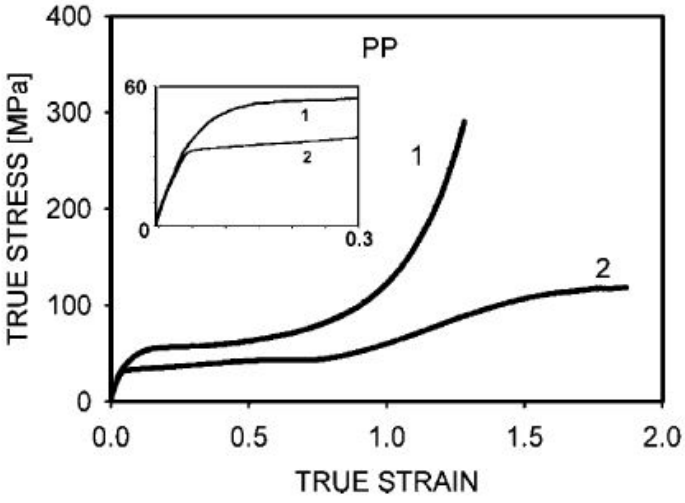

Figure 1.2: *The difference in compression(1) and tension(2) for i-PP [6].*

To quantify the voiding in the amorphous phase, a voiding model is added to the EGP part of the CIM. In this case, a Gurson model [8, 9] was chosen for it's micromechanical derivation and extendibility, due to further work from numerous authors [10–23]. To do this, certain derivations were made to ensure the convergence of the CIM. Certain constitutive relations will also had to be altered to account for the hydrostatic contribution to the deformation, accompanied by voiding. These changes will be discussed in Section 4.
In Section 5 the trends of the model including voiding will be shown. These results will be compared to the limitted data available for the material under review, α-phase i-PP. The conclusions and recommendations will be given in the last Section, 6.

2 Semi-Crystalline polymers

Semi-crystalline polymers are polymers which consist of two phases, an amorphous phase and a crystalline phase. These phases show different behaviour. The amorphous phases are regions where the molecular chains do not show any order. The crystalline phase shows highly ordered chains. This results in the amorphous phase showing an isotropic elasto-viscoplastic response and the crystalline phase an anisotropic elasto-viscoplasitc response. The anisotropy of the crystalline phase is caused by the ordered chains, resulting in yield dependent on the loading direction.
One advantage of this semi-crystalline structure in a product is the ability to use the polymer up to the melting temperature, whereas amorphous polymers are subjected to the glass transition temperature [24]. The material that is currently being investigated is isotactic poly-propylene (iPP). The material characteristics of this polymer are highly dependent on the processing conditions. There are several phases that the polymer can consist from. The composition of the phases in the polymer are determined by the processing conditions. The phases that can occur are α, β, γ and meso-phase. The conditions that determine the growth of these crystals are the cooling rate from the melting point, the flow in the material and the pressure during cooling. Using a fast cooling rate results in a mesophase structure. By inducing flow in the material, the growth of α and β phase can be enhanced. γ growth responds to higher pressures. The temperature and pressure dependence can be seen in Figure 2.1 [25].

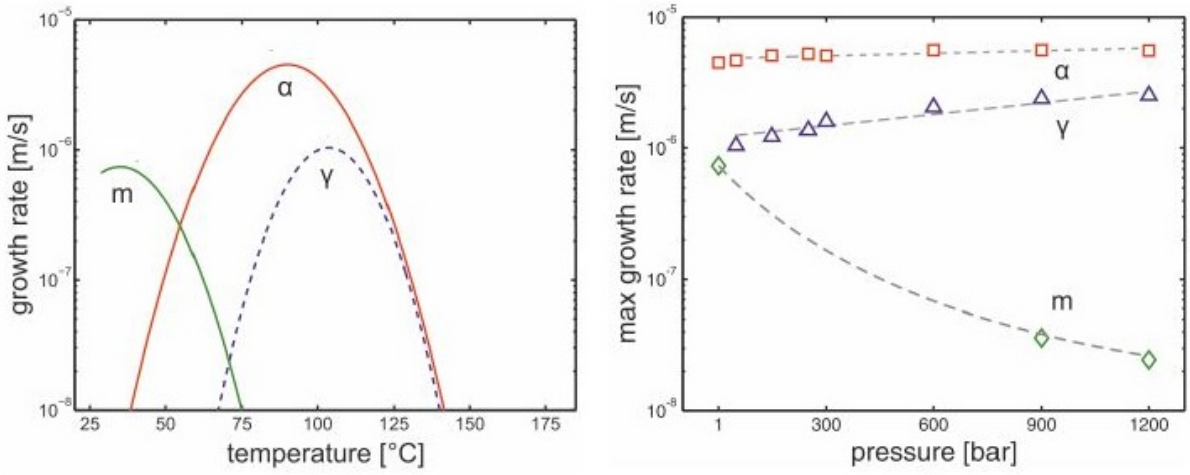

Figure 2.1: *Results for processing condition experiments for phase growth [25].*

The phase composition of the polymer determines ultimately what the characteristics are. This is also shown in the results of Caelers et al [7] , which show a different stress-strain response and also different voiding behaviour. This will be discussed in Section 2.3.
Flow in the polymer will give rise to orientation in the direction of the flow. A material not subjected to flow will have a spherulitic structure as shown in Figure 2.2. With increasing flow, a more oriented structure will occur. If the polymer is oriented enough a so-called shish-kebab structure will be formed.

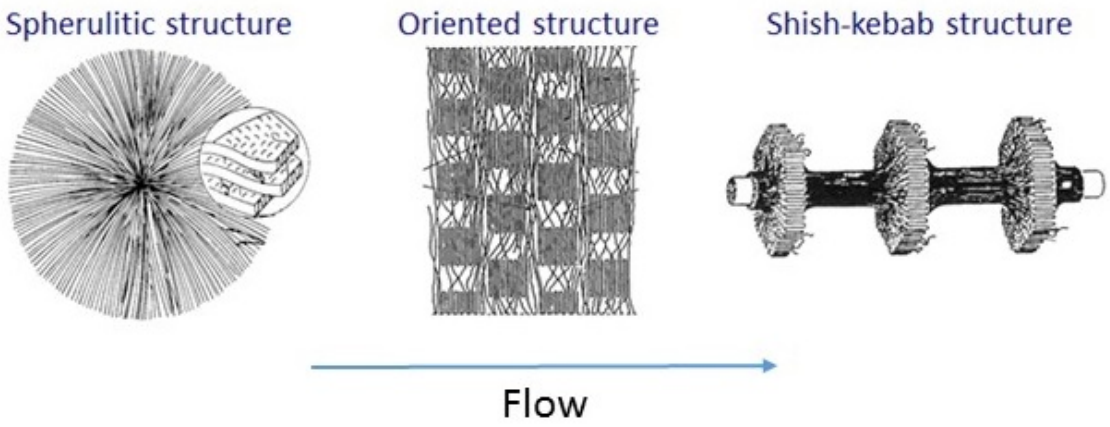

Figure 2.2: *Orientation evolution due to flow from spherulitic (Lin & Argon [26]), oriented structure (Gohil [27]) and a shish-kebab structure (Barham & Keller [28]).*

Regardless of the orientation the amorphous and crystalline layers will be stacked. This allows the modelling of the material using stacked phases of a crystalline and amorphous phase, as will be discussed in Section 3.3.
The orientation of this structure has a high influence on the characteristics of the polymer. With the molecular chains located in the direction of the applied flow the material will show a different behaviour loading in this direction compared to loaded perpendicular to the orientation. This was shown by van Erp [29] with injection moulding i-PP. The yield stress showed dependence on the orientation of the sample compared to the flow direction. These results are shown in Figure 2.3. It can be seen that the yield stress is highly dependent on the orientation of the crystals in the samples.

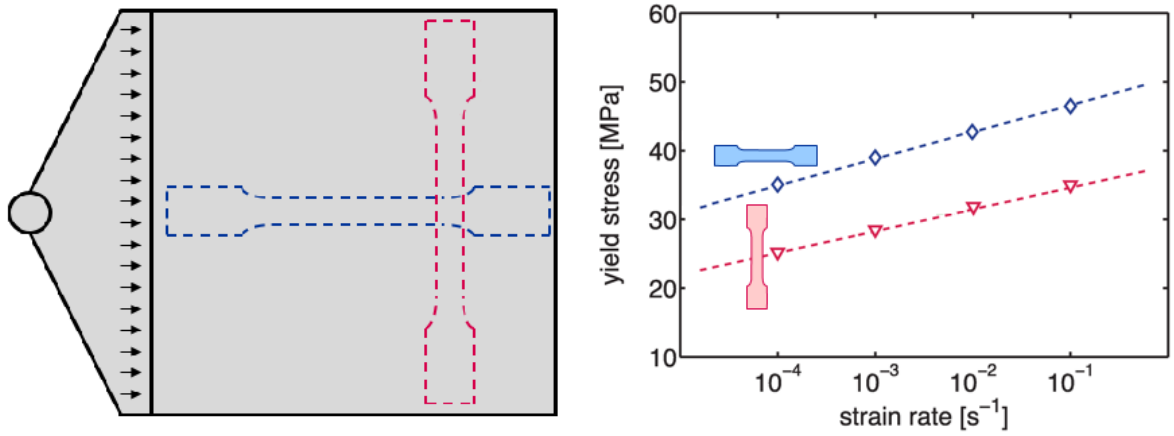

Figure 2.3: *A schematic representation of the injection moulding of the samples with the yield kinetics during tensile testing [29].*

These yield kinetics can be described by looking at the deformation characteristics of both phases. They deform differently and with different mechanisms.

2.1 Crystalline phase deformation

The plastic deformation in the crystalline phase takes place due to crystallographic slip, mechanical twinning and stress-induced martensitic transformation. However, the main deformation mechanism is crystallographic slip [1, 26, 30–32]. Crystallographic slip is the sliding of chains over slip planes. Over these slip planes there can be transverse slip, perpendicular to the chain direction, and chain slip, in the chain direction. The slip systems are material dependent. For α phase i-PP these slip systems are shown in Figure 2.4. α i-PP shows a monoclinic crystal structure [7].

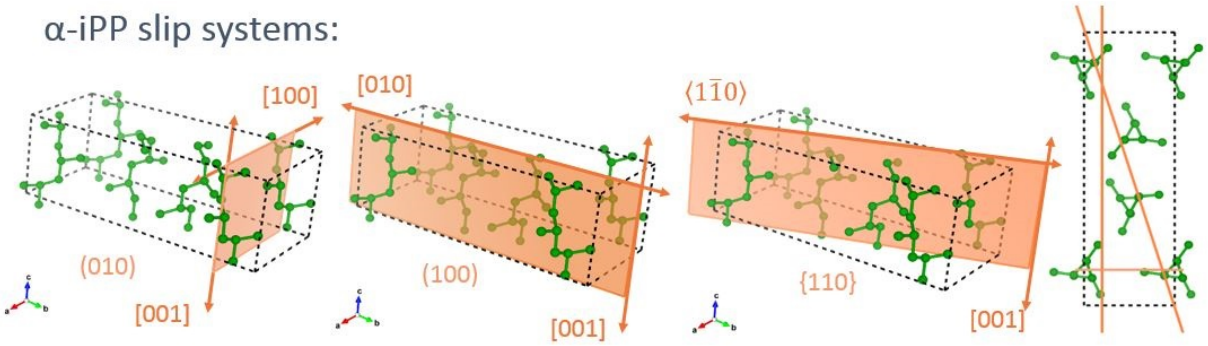

Figure 2.4: *The slip systems of i-PP with transverse slip [XX0] and chain slip [001].*

Slip can be either fine slip or coarse slip. Fine slip is defined as equal deformation over a large amount of slip planes. Coarse slip occurs at high strains which shows large slips over a small number of planes [26]. These forms of slip are shown in Figure 2.5.

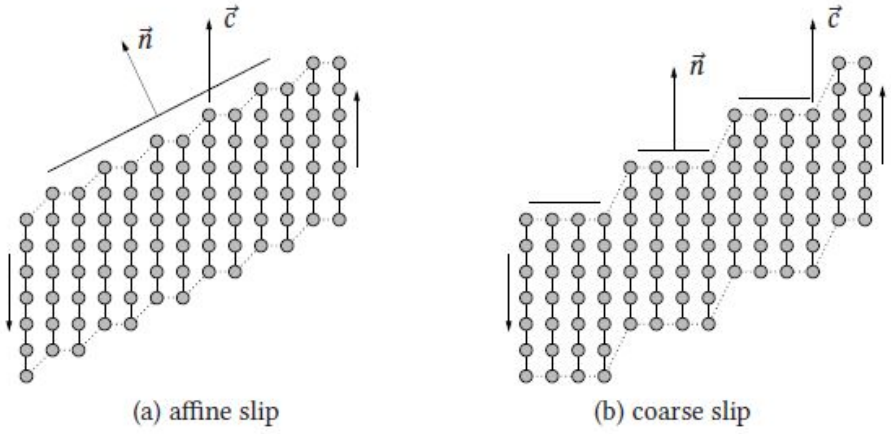

Figure 2.5: *Schematic representation of slips [2], after Young [30].*

As is displayed in Figure 2.5 the interface normal, n, changes during fine slip while the chain direction remains the same. This interface normal is the normal between the amorphous and crystalline phases. The modelling of the crystal phase is further explained in Section 3.2.

2.2 Amorphous phase deformation

For α i-PP, with a crystallinity of 60%, the amorphous phase will transition to a glassy state at a temperature of 15°C [7]. Above this temperature, the amorphous phase will be in the rubbery state. During the plastic deformation of a semi-crystalline polymer, voiding may occur in the amorphous phase. Voiding happens when the material is placed under a tensile stress, due to a negative hydrostatic stress. In compression, there is no voiding due to a positive hydrostatic stress. When there are voids present, these can shrink or collapse due to this positive stress. Voiding starts to show prior to yielding in i-PP [7]. This is however found to be dependent on the phase and processing conditions of the material [32]. For example, the temperature has a large influence on voiding [7, 32, 33]. This also shows in the reduced yield stress. The voiding has a large impact on the stress-strain response of the material. This impact can easily be seen when comparing a compression test and a tensile test. This is visualized in Figure 2.6. Prior to voiding, the plastic deformation of the material is driven through the deviatoric stress, independent of the hydrostatic stress [34].
As can be seen in Figure 2.6 there is an initial difference in material response between compression and tension, while there is no sign of voiding yet. This is likely due to other damage mechanisms and while the addition of voiding to the CIM will improve the tension response. This will likely show the same difference as voiding in the model appears close to yield. This difference could however also be due to a difference in experimental conditions.

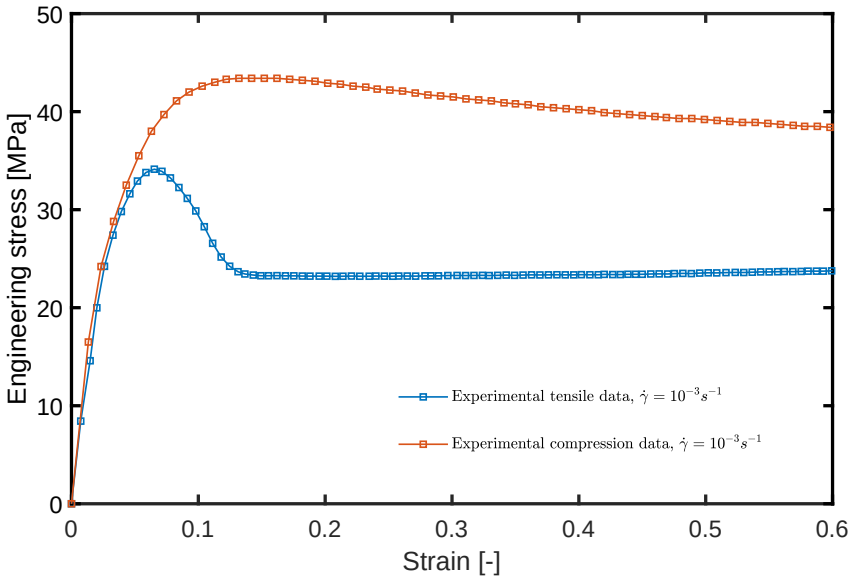

Figure 2.6: *The experimental stress-strain response of α i-PP by Caelers [7] at 23°C, strain-rate 10^{-3} s^{-1}.*

It can be seen that there is a large decrease in yield stress and a large increase in softening. While this is also caused by necking of the material, Chu et al. [33] found that β i-PP showed no necking at higher temperatures, but did show voiding. Comparing this to the results of Caelers et al. [7], the β i-PP samples showed an increased softening response and less hardening during tensile loading. Using SAXS, voiding has been studied [6, 7, 32, 35, 36], see Figure 2.7. From these measurements the void shape evolution and strains where voiding occurs can be seen. With increasing strain the voids will grow and new voids will start to appear. At nucleation the voids will grow perpendicular to the tensile direction. After yielding these voids will start to grow in the tensile direction. This is observed in multiple measurements [6, 7, 35, 37]. The matrix between the voids starts to thin during growth. This then leads to the coalescence of voids. Coalescence results in fast breaking of the material, in the order of 10-15% void fraction for metals [10]. Voiding can sometimes also be seen as whitening near the yield point [5, 32, 37]. This whitening is caused

by numerous small voids.
Whether the nucleation of voids precedes or is caused by lamellar fragmentation is debatable [6, 35]. The slip in crystalline lammellae does leave room for void growth in the amorphous phase, with thicker lamellae causing higher void nucleation. However, Pawlak and Galeski [39] found that crystalline destruction following voiding in the amorphous phase was more likely due to the stress release during crystal fragmentation, decreasing the local stress [6]. Selles found that voids appear in the equatorial plane and polar fans of a spherulite while keeping the centre intact [40].

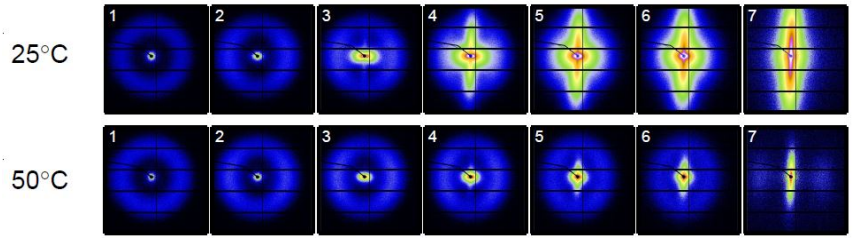

Figure 2.7: *SAXS results found by Caelers [7].*

There are however two forms of void forming. The first is the voiding around yield, as discussed. The second voiding process is at larger strain due to disentanglement of the network [37]. These voiding processes appear to be independent of each other and the molecular weight seems to be of high influence on this mechanism. However, in this work the focus is on the void growth around yield, rather than disentanglement.
Several works looked at cavitation in i-PP under tension [6, 32, 33, 37–39]. These works, however, did not show actual porosities of the material. While Chu et al. [33] did show porosity, these porosities were for β i-PP samples and did not show the evolution during strain. Since the material under review is α i-PP, these results can not readily be used. One work showing these porosities for different processing conditions, including α i-PP, is Caelers et al [7]. While these results are not completely relatable, the porosities can be compared.

2.3 Experimental Results

There is little experimental data available in literature for voiding in i-PP. Fortunately there was a study done by Caelers et al. which tested the material behaviour in both tension and compression for i-PP. They also looked at the differences between α, β and γ i-PP. Furthermore the influence of strain-rate and temperature was investigated. Additionally, in tension also the porosity was measured. The results for the tensile test measuring porosity are shown below:

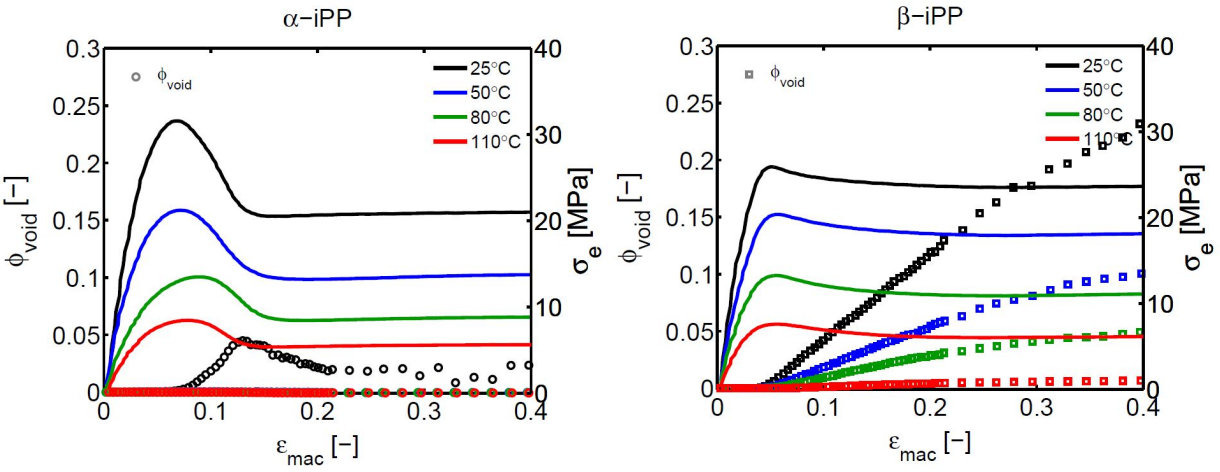

(a) *Tensile test α i-PP*

(b) *Tensile test β i-PP*

(c) *Tensile test γ i-PP*

Figure 2.8: *The results found by Caelers [7], strain rate $8{\cdot}10^{-4}$ s^{-1}.*

These results show the tensile response for α, β and γ i-PP's. While only α i-PP is used currently, the experimental results of the two other phases show a more fluent porosity evolution. This is likely due to the voids in α i-PP growing too fast to the point where they can not be measured by SAXS (Small Angle X-ray Scattering) measurements. The voids that become too big will therefore not be taken into account, resulting in a decrease in the measured porosity. While there is an initial decrease the porosity remains more or less constant afterwards. This could mean that there is a constant amount of nucleated voids. A similar constant porosity is observed in β and γ i-PP. However, they remain constant at their respective maximum levels of porosity. Collapsing of voids due to decreased hydrostatic stress could be a reason for these drops in void growth according to Caelers.
While α i-PP is used the void growth in the other phase i-PP's show better trends, since in α there is only growth noticeable in the 25°C case. However, the other temperature cases still show a lot of softening and

no hardening after yield. This is probably due to voids. These might not be measured as the materials resilience against stress at elevated temperatures decreases, giving possibility to faster growths. This could render the voids undetectable by SAXS as discussed.
Another thing that should be taken into account when comparing results is the fact that these measurements were done in a standard tensile test, clamping the sample at both ends, and measuring the force and strain. However, in the CIM a material point is simulated, comparable to a point in the middle of the sample where yield takes place, see Figure 2.9. This difference is caused by necking, resulting in a high local stress. Therefore these results are not perfectly comparable, as the CIM will likely result in higher stress and this will therefore also influence the voiding results.

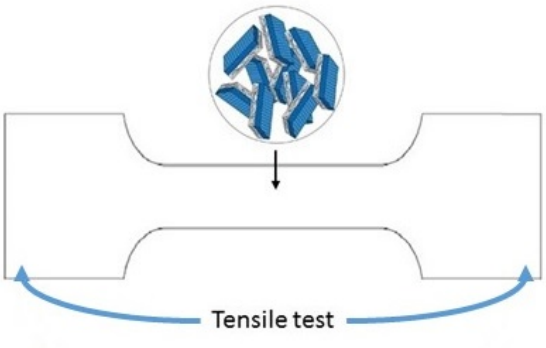

Figure 2.9: *Caelers tests vs the CIM.*

3 The Composite Inclusion Model

Modelling the characteristics of a semi-crystalline polymer is necessary to predict material properties under different processing and loading conditions. As dicussed in Section 2, a semi-crystalline polymer consists of two separate phases with both different deformation characteristics. The behaviour of these phases should therefore also be modelled separately. To this extend the Composite Inclusion Model (CIM) was made, which combines the different responses into a single model.

3.1 The Amorphous Phase

The amorphous phase shows an isotropic elasto-viscoplastic response. This response can be modelled using the EGP model. This model was developed by Tervoort et al. [4], Govaert et al. [41], Klompen [42] and van Breemen et al. [43]. The model uses multiple Maxwell models to model the elasto-viscoplastic behaviour. The hardening of the material is modelled using a single hardening spring. This model is shown in Figure 3.1a. Maxwell modes can be added with their respective parameters to describe the material characteristic up to the yield point better. As semi-crystalline polymers can show α, β and γ phases with different behaviours, multiple mechanism have to be modelled. These mechanisms can be added as additional modes, as shown in Figure 3.1b.

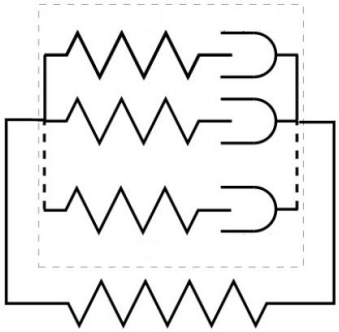

(a) *Single process model*

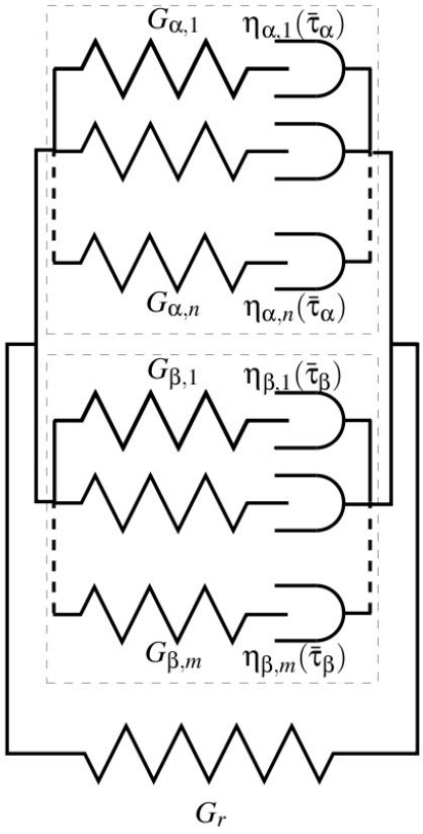

(b) *Multiple process model*

Figure 3.1: *Representations of the EGP model [44].*

The EGP model uses a modified Eyring flow rule to describe the viscoplastic behaviour of the material. In these Eyring equations, the viscosity was extended, to include the pressure dependence and the aging

effect. This results in the following equation for the plastic deformation rate:

$$\boldsymbol{D}_p = \frac{\boldsymbol{\sigma}_s^d}{2\eta}. \tag{3.1}$$

This overall plastic deformation rate is defined using the deviatoric driving stress, $\boldsymbol{\sigma}_s^d$ and viscosity η of the mode with the highest viscosity. The plastic spin is set to zero, resulting in the plastic velocity gradient being equal to the plastic deformation rate. The driving stress is defined by a hydrostatic and a deviatoric part:

$$\boldsymbol{\sigma}_s = \boldsymbol{\sigma}_s^h + \boldsymbol{\sigma}_s^d = \kappa(J_e - 1)\mathbf{I} + \sum_{n}^{i=1} G_i \tilde{\mathbf{B}}_{e,i}^d, \tag{3.2}$$

with n being the number of Maxwell modes, J_e being the volumetric change of the material, κ the bulk modulus and G the shear modulus. $\tilde{\mathbf{B}}_{e,i}^d$ is the deviatoric part of the elastic isochoric left Cauchy-Green strain tensor. The viscosity including the pressure and ageing influences is defined as:

$$\eta_i = \eta_{0,i,ref} \frac{\frac{\tau}{\tau_0}}{\sinh(\frac{\tau}{\tau_0})} \exp(\frac{\mu P}{\tau_0}) \exp(S_a R(\gamma_p)). \tag{3.3}$$

$\eta_{0,ref}$ is defined as the viscosity in the rejuvenated state [42]. The pressure (P) is defined as $-\kappa(J_e - 1)$, J_e being the elastic volumetric change of the first mode. τ_0 is the characteristic stress, μ the pressure dependancy parameter, S_a the aging parameter. $R(\bar{\gamma_p})$ is the softening function, which is fitted to describe the softening of the material. This parameter reduces from 1 to 0 over $\bar{\gamma_p}$, decreasing the effect of the aging parameter [43]. This softening function is defined as:

$$R(\bar{\gamma_p}) = \frac{(1 + (r_0 \exp(\bar{\gamma_p}))^{r_1})^{(r_2-1)/r_1}}{(1 + r_0^{r_1})^{(r_2-1)/r_1}}, \tag{3.4}$$

where r_0, r_1 and r_2 are fitting parameters. The equivalent stress τ is defined as $\sqrt{\frac{1}{2}\boldsymbol{\sigma}_s^d : \boldsymbol{\sigma}_s^d}$ and the equivalent plastic strain rate $\dot{\bar{\gamma}}_p$ can be defined as $\frac{\tau}{\eta}$. Both $\dot{\bar{\gamma}}_p$ and τ are defined over the mode with the highest viscosity.
The hardening of the material is described using the deviatoric part of the total isochoric left Cauch-Green strain tensor, $\tilde{\mathbf{B}}^d$, and a hardening modulus G_r:

$$\boldsymbol{\sigma}_r = G_r \tilde{\mathbf{B}}^d. \tag{3.5}$$

The total stress is defined as an addition of the driving and hardening stress:

$$\boldsymbol{\sigma} = \boldsymbol{\sigma}_r + \boldsymbol{\sigma}_s. \tag{3.6}$$

3.2 The Crystalline Phase

The crystalline phase also consists of an elastic part and a viscoplastic part. The elastic part can be modelled using a linear relation between the elastic Green-Lagrange strain tensor $\mathbf{E}_e$ and the elastic second Piola-Kirchhoff stress $\mathbf{S}$. This is done using an anisotropic elastic modulus tensor ${}^4\mathbf{C}$. This tensor is anisotropic as the chain will have a higher modulus in the chain direction. This leads to the following relation:

$$\mathbf{S} = {}^4\mathbf{C} : \mathbf{E}_e, \tag{3.7}$$

with $\mathbf{S}$ being defined as:

$$\mathbf{S} = J_e \mathbf{F}_p^{-1} \cdot \boldsymbol{\sigma} \cdot \mathbf{F}_e^{-T}. \tag{3.8}$$

$\mathbf{F}_e$ is defined as the elastic deformation gradient and the elastic volumetric change J_e as its determinant. $\mathbf{F}_p$ is then defined as the plastic deformation gradient. $\mathbf{E}_e$ is defined as:

$$\mathbf{E}_e = \frac{1}{2}(\mathbf{F}_e^T \cdot \mathbf{F}_e - \mathbf{I}), \tag{3.9}$$

with $\mathbf{I}$ being the second order identity tensor.
The majority of deformation in the viscoplastic part is due to crystallographic slip for moderate strains, see Section 2.1. Therefore this is assumed as the main deformation mechanism in the crystalline phase. In the model, currently only fine slip is included, while in reality also coarse slip may occur. Since coarse slip becomes important at large strains it is assumed that the deformation comes from fine slip. In Figure 2.5, these slip mechanisms are shown schematically. With fine slip, the chain direction angle changes.
To model the crystallographic slip a rate dependent crystal plasticity model is used. The deformation in every slip system is taken into account, leading to the following plastic velocity gradient:

$$\mathbf{L}_p = \sum_{i=1}^{N} \dot{\gamma}^i \vec{s}_0^{\,i} \otimes \vec{n}_0^i, \tag{3.10}$$

with N the amount of slip systems, 8 for iPP, $\vec{s}_0$ the unit slip direction and $\vec{n}_0$ the unit slip plane normal. $\vec{s}_0$ and $\vec{n}_0$ are also displayed in Figure 2.5. $\dot{\gamma}^a$ is defined as the shear rate of the slip system. This shear rate is defined using an Eyring flow rule [24]:

$$\dot{\gamma}^i = {\dot{\gamma}_0}^i \exp(\frac{-\Delta U^i}{RT}) \sinh(\frac{\tau^i}{\tau_0^i}) \exp(\frac{\mu^a \sigma_n^i}{\tau_0^i}). \tag{3.11}$$

Here ${\dot{\gamma}_0}^i$ is the reference shear rate, with τ_0^i the reference shear strength. ΔU is the activation energy of the slip system, with R; the gas constant, and T; the temperature in Kelvin. $\boldsymbol{\sigma}_n^i$ is the normal stress of the slip plane with μ^i its dependency parameter. τ^i and σ_n^i can be calculated using the second Piola-Kirchhoff stress, given in Equation 3.8. This results in the following relation for τ^i:

$$\tau^i = \mathbf{S} \cdot \mathbf{C}_e^c : (\vec{s}_0^{\,i} \otimes \vec{n}_0^i), \tag{3.12}$$

with $\mathbf{C}_e^c$ the elastic right Cauchy-Green deformation tensor. σ_n^i is defined as:

$$\sigma_n^i = S : (\vec{n}_0^i \otimes \vec{n}_0^i). \tag{3.13}$$

Equation 3.11 describes the plastic deformation for a single relaxation mechanism. However, as a single mechanism is not able to fully describe the deformation, another mechanism is present in the model. These mechanisms can be added into a single term [24]. This was fist employed by Sedighiamiri for the combination of mechanisms in both the crystalline and amorphous phase. Using a Ree-Eyring [45] flow rule the shear stress was altered to take both mechanisms into account. In case two mechanisms are used the following shear rate description is obtained:

$$\dot{\gamma} = \frac{\dot{\gamma_0}^{a,I} \exp(\frac{-\Delta U^{a,I}}{RT}) \sinh(\frac{\tau}{\tau_0^{a,I}}) \dot{\gamma_0} \sinh(\frac{\tau}{\tau_0^{a,I+II}})}{\dot{\gamma_0}^{a,I} \exp(\frac{-\Delta U^{a,I}}{RT}) \sinh(\frac{\tau}{\tau_0^{a,I}}) + \dot{\gamma_0}^{a,I+II} \sinh(\frac{\tau}{\tau_0^{a,I+II}})} \exp(\frac{\mu \sigma_n}{\tau_0^a}), \tag{3.14}$$

with

$$\tau_0^{a,I+II} = \tau_0^{a,I} + \tau_0^{a,II}, \tag{3.15}$$

and

$$\dot{\gamma_0}^{a,I+II} = 2 \exp(-\frac{\tau_0^{a,I} \ln(\frac{2}{\gamma_0^{a,I}} \exp(\frac{\Delta U^{a,I}}{RT})) + \tau_0^{a,II} \ln(\frac{2}{\gamma_0^{a,II}} \exp(\frac{\Delta U^{a,II}}{RT}))}{\tau_0^{a,I} + \tau_0^{a,II}}). \tag{3.16}$$

As mentioned, this was first employed by Sedighiamiri for the amorphous phase. This, however, was not included yet in the model as the amorphous model allowed for separate modes, instead of combining them into one.

3.3 Combining the models

To model a semi-crystalline polymer these two phases have to be combined. Combining them into a layered structure, results in a microscopic scale model. This is done to model the elasto-viscoplastic deformation behaviour, which semi-crystalline polymers show. These models consist of one amorphous phase and one crystalline phase, see Figure 3.2a. One of these coupled structures is called a "Composite Inclusion". The model uses a mean field approach to determine the characteristics of the polymer. This is done by using multiple inclusions, a collection of these inclusions is an aggregate, see Figure 3.2b. The ratio of the amorphous to crystalline phase can be changed, depending on the material that is used. This layered structure was first proposed by Lee et al. [1]. This model was then further extended by the addition of several phenomena to be able to capture the semi-crystalline polymer under investigation.

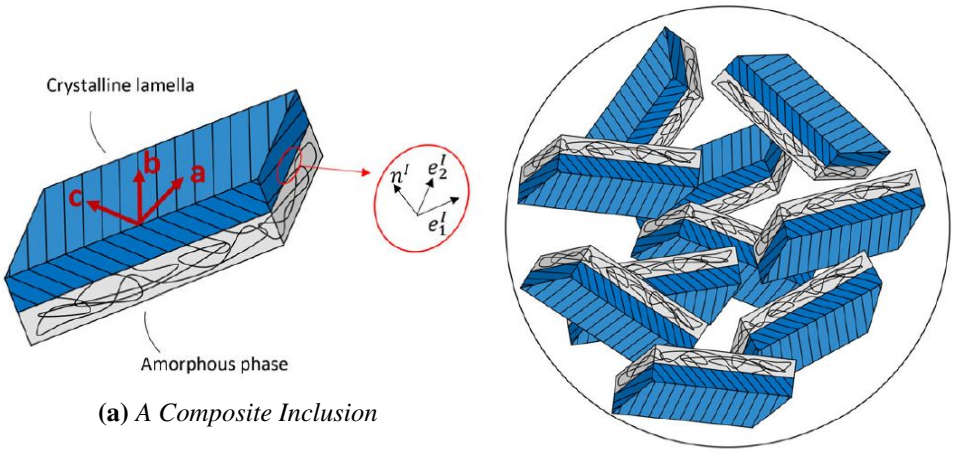

(a) *A Composite Inclusion*

(b) *An aggregate*

Figure 3.2: *A representation of the CI model for PE [46].*

The phases are coupled at the interface. There is no mass flux over the phases and at the interface a traction equilibrium is assumed, as well as kinematic compatibility. These last two conditions make sure that the material deforms equaly at the boundary and that the stress is equal at the boundary. These conditions can be described as follows:

$$\mathbf{F}^c \cdot \vec{x}_0^I = \mathbf{F}^a \cdot \vec{x}_0^I = \mathbf{F}^I \cdot \vec{x}_0^I, \tag{3.17}$$

$$\boldsymbol{\sigma}^c \cdot \vec{n}^I = \boldsymbol{\sigma}^a \cdot \vec{n}^I = \boldsymbol{\sigma}^I \cdot \vec{n}^I, \tag{3.18}$$

with $\vec{x}_0^I$ being an arbitrary vector in the interface plane and $\vec{n}_0^I$ the interface normal. Over the inclusion, the stress and deformation are assumed homogeneous within each phase. The total stress and deformation are therefore volume averaged over each inclusion. This is done using the volume fraction of each phase, by calculating the average over the volume. For the stress, the elastic dilatation of the phases has to be taken into account [2]. Taking this into account this leads to the following evolution of volume fractions:

$$f^\pi = \frac{f_0^\pi J^\pi}{f_0^a J^a + f_0^c J^c}; \qquad \pi = a, c. \tag{3.19}$$

Here J is defined as the determinant of $\mathbf{F}$. Using this compensation the following expressions for deformation and stress of the inclusions are obtained:

$$\mathbf{F}^I = f_0^a \mathbf{F}^a + f_0^c \mathbf{F}^c, \tag{3.20}$$

$$\boldsymbol{\sigma}^I = f^a \boldsymbol{\sigma}^a + f^c \boldsymbol{\sigma}^c. \tag{3.21}$$

Going from a microscopic to a mesoscopic scale an interaction law has to be formulated between the inclusions. In the model a hybrid interaction law is used. This describes an interaction between the upper bound Taylor and lower bound Sachs interactions [1, 2]. For this model six additional "stretchlike" variables are introduced. The interface conditions are then defined as follows:

$$ {}^4\mathbf{P}^{I^i}_{x_0} : \mathbf{F}^{c^i} =^4 \mathbf{P}^{I^i}_{x_0} : \mathbf{F}^{a^i} = \mathbf{P}^{I^i}_{x_0} : \mathbf{F}^{I^i} \tag{3.22} $$

$$ {}^4\mathbf{P}^{I^i}_{n} : \boldsymbol{\sigma}^{c^i} =^4 \mathbf{P}^{I^i}_{n} : \boldsymbol{\sigma}^{a^i} = \mathbf{P}^{I^i}_{n} : \boldsymbol{\sigma}^{I^i} \tag{3.23} $$

The mesoscopic relations are then described using a Sachslike interaction law for the stretch, and a Taylorlike relation for the stress:

$$ {}^4\mathbf{P}^{I^i}_{x} : \boldsymbol{\sigma}^{I^i} =^4 \mathbf{P}^{I^i}_{x} : \bar{\boldsymbol{\sigma}}, \tag{3.24} $$

$$ {}^4\mathbf{P}^{I^i}_{n_0} : \mathbf{U}^{I^i} =^4 \mathbf{P}^{I^i}_{n_0} : \hat{\mathbf{U}}, \tag{3.25} $$

$$ \mathbf{R}^{I^i} = \bar{\mathbf{R}}; \qquad i = 1 : N_I. \tag{3.26} $$

Here $\bar{\mathbf{R}}$ is the mesoscopic rotation, $\bar{\boldsymbol{\sigma}}$ the mesoscopic stress and $\hat{\mathbf{U}}$ are the "stretchlike" unknowns. ${}^4\mathbf{P}^{I^i}$ is the subspace projection of the inclusion-averaged variables on the mesoscopic result. The model can be solved by imposing a set of boundary conditions, resulting in a set of unknowns. On this set certain boundary conditions are imposed. For an uniaxial loading case, loaded in the e_1 direction, which is under consideration here, the conditions are obtained:

$$ \bar{\mathbf{R}} = \mathbf{I}, \tag{3.27} $$

$$ \bar{U}_{11} = \lambda(t), \tag{3.28} $$

$$ \bar{\sigma}_2 2 = \bar{\sigma}_3 3 = \bar{\sigma}_1 2 = \bar{\sigma}_1 3 = \bar{\sigma}_2 3 == 0. \tag{3.29} $$

Here λ is the imposed stretch. This set of introduced "stretchlike" unknowns in then solved using a Newton-Raphson method.

Under deformation a texture evolution occurs. In the model this is incorporated through changes in crystalline lamellae orientation and morphological texture changes [24]. The morphological texture changes are the changes in interface orientation between the crystal and amorphous phase. This morphological texture is constant during the increment of calculation and is updated afterwards. This is done by updating the interface normal.

The update of this normal is defined using two independent vectors in the interface, $\mathbf{x}_1^{I^i}$ and $\mathbf{x}_2^{I^i}$. These are defined using the same vectors, at $t = 0$:

$$ \mathbf{x}_1^{I^i} = \mathbf{F}^i \cdot \mathbf{x}_{01}^{I^i}, \tag{3.30} $$

with $\mathbf{x}_{01}^{I^i}$ and $\mathbf{x}_{02}^{I^i}$ the vectors at $t = 0$. The interface normal $\mathbf{n}^{I^i}$ is then calculated as:

$$ \mathbf{n}^{I^i} = \frac{\mathbf{x}_1^{I^i} \times \mathbf{x}_2^{I^i}}{||\mathbf{x}_1^{I^i} \times \mathbf{x}_2^{I^i}||}. \tag{3.31} $$

In the model, uniaxial tension or compression can be described on the aggregate. This is done by means of a constant prescribed strain rate. A Newton-Raphson procedure is then utilised to calculate the deformations and stresses.

4 The Gurson model

As discussed, voiding occurs in iPP under a tensile stress, see Section 2. Voiding occurs in the amorphous phase. Since this affects the load carrying ability of the amorphous phase, voiding is added by altering the EGP part of the CIM. Incorporating the effects of voiding can be done by means of the Gurson model [8,9]. Gurson first developed this micromechanical approach for voiding in steel. However, the model has numerous extensions to improve the response. Due to the extensibility and the ease of implementation this work was chosen to model the voiding.

4.1 Defining the model

The original Gurson model was derived for the modelling voiding in ductile materials, more specifically steel. It is derived using a micro-mechanical approach. Since the von Mises criterion assumes incompressible material, which is not the case during voiding, hydrostatic dependence should be taken into account. The Gurson model approximates the yield criterion while including hydrostatic stress. This approximation is done by adapting the yield surface of the material. It, however, is based on spherical or cylindrical voids and can only describe growth in already existing voids in isotropic materials, see Figure 4.1.

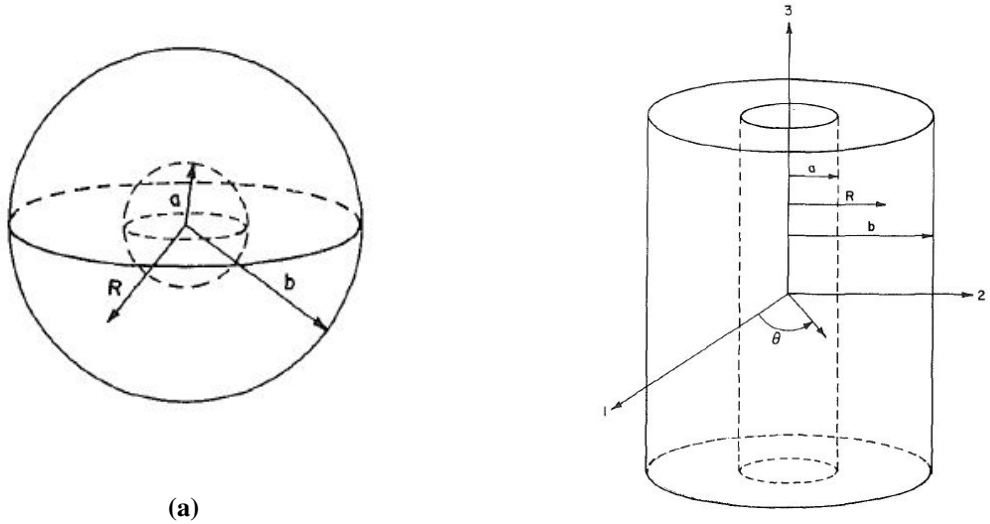

(a) **(b)**

Figure 4.1: *The voids as used in Gurson's model [8]*

Gurson formulated a potential for the model to adapt the yield surface. At yield this potential would be zero. In this potential the effects of the porosity of the material, or void fraction, and the hydrostatic stress were included. The void fraction is defined as:

$$f = \frac{V_{voids}}{V_{matrix}}. \tag{4.1}$$

The potential proposed by Gurson for spherical voids is the following [9]:

$$\Phi = \frac{1}{2}\frac{\Sigma_{eqv}^2}{\sigma_y^2} + 2f\cosh(\frac{\sqrt{3}}{2}\frac{\Sigma^h}{\sigma_y}) - (1+f^2) = 0. \tag{4.2}$$

This potential is an upper bound yield criterion. The criterion given here is based on spherical voids and is based on yield stress, σ_y, the equivalent macroscopic stress Σ_{eqv} and the hydrostatic stress Σ^h. This

equivalent and hydrostatic stresses for the potential are defined as:

$$\Sigma_{eqv} = \sqrt{\frac{3}{2}\bar{\boldsymbol{\sigma}}^d : \bar{\boldsymbol{\sigma}}^d}, \tag{4.3}$$

$$\Sigma^h = \frac{1}{3} tr(\bar{\boldsymbol{\sigma}}), \tag{4.4}$$

This potential is shown in Figure 4.2 for various porosities.

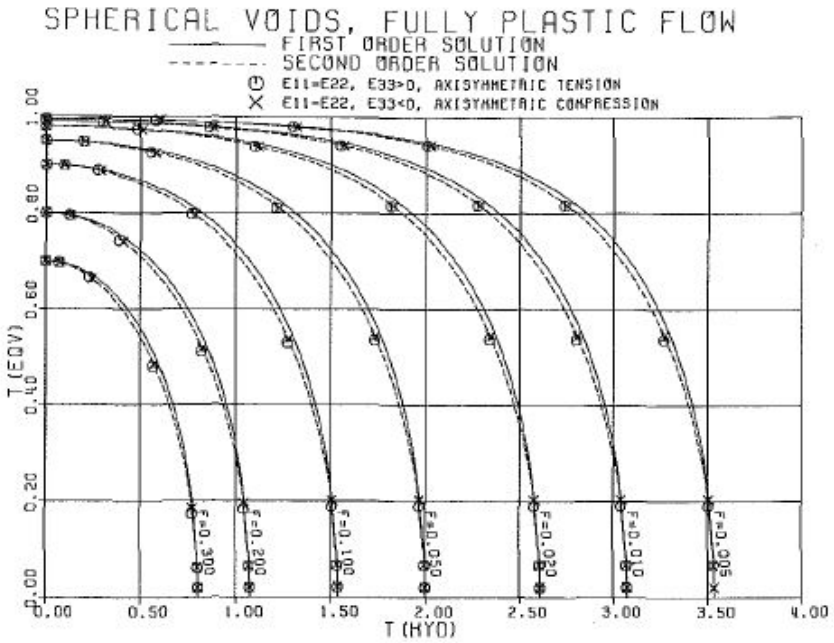

Figure 4.2: *The yield surface for various porosities [8].*

It can be seen that the maximum stress, both equivalent and hydrostatic decrease with increasing porosity. Here T_{eqv} and T_{hyd} are Σ_{eqv} and Σ^h normalised with the yield stress σ_y, respectively.
One work incorporating the Gurson model for glassy polymers is Steenbrink [47]. Steenbrink introduced a Gurson framework in a elasto-viscoplastic material. Following this work the following potential is used:

$$\Phi = \frac{1}{2}\frac{\bar{\boldsymbol{\sigma}}^d : \bar{\boldsymbol{\sigma}}^d}{\tau^2} + 2f\cosh(\frac{\sqrt{3}}{2}\frac{\frac{1}{3}tr(\bar{\boldsymbol{\sigma}})}{\tau}) - (1+f^2) = 0. \tag{4.5}$$

Here f is the porosity, $\frac{1}{3}tr(\bar{\boldsymbol{\sigma}})$ the hydrostatic stress and τ the equivalent shear stress rather than the yield stress proposed by Gurson. τ is variable, calculated according to the potential. The implementation of this will be discussed in Section 4.1.1. The plastic deformation rate is described as follows:

$$\mathbf{D}_p = \dot{\Lambda}\frac{\partial \Phi}{\partial \bar{\boldsymbol{\sigma}}}. \tag{4.6}$$

$\dot{\Lambda}$ is found by setting the dissipation equal to the plastic work rate. This gives the following expression:

$$\dot{\Lambda} = (1-f)\tau\dot{\gamma}^p(\bar{\boldsymbol{\sigma}} : \frac{\partial \Phi}{\partial \bar{\boldsymbol{\sigma}}})^{-1}, \tag{4.7}$$

with $\dot{\gamma}_p$ the equivalent plastic strain rate. The formulation presented here differs from the Steenbrink et al. formulation. Steenbrink et al. defined $\dot{\Lambda}$ with a factor $\sqrt{2}$, but due to a different formulation of $\dot{\gamma}$ this factor drops out. In the original EGP model, the plastic deformation rate is defined as:

$$\mathbf{D}_p = \frac{\dot{\gamma}_p}{\tau}\boldsymbol{\sigma}^d. \tag{4.8}$$

Without voiding present in the model, the plastic deformation rate description should reduce to the old form, shown above. With a porosity, f of 0, the equivalent stress remains defined as:

$$\tau = \sqrt{\frac{1}{2}\boldsymbol{\sigma}^d : \boldsymbol{\sigma}^d}, \tag{4.9}$$

with $\boldsymbol{\sigma}^d$ the deviatoric stress. This indeed results in Equation 4.6 being equal to 4.8.

4.1.1 Implementation

To implement the defined model into the existing CIM some changes have to be made. These changes were made to the EGP part, where voiding normally occurs. Implementing this in the EGP model is done through the velocity gradient tensor. This is set equal to the plastic deformation rate as plastic rotation is assumed to be zero.
The equivalent stress is defined such that the potential remains zero. This can be done using a Newton-Raphson method. Altough both the CIM and the EGP model use Newton-Raphson methods to calculate the stresses, the CIM Newton-Raphson remains the same.
The initial guess for the first increment of the model remains defined as equation 4.9. This is due to the equivalent stress reducing to 4.9, and $\mathbf{D}_p$ resulting in 4.8, when the porosity is 0. In new increments the equivalent stress of the previous increment is used as the initial guess. This reduces the amount of iterations needed at rising void fractions, where the equivalent stress calculated to keep the potential zero will increase over the old definition, Equation 4.9. The new Newton-Raphson procedure was defined as follows:

$$\Phi(\tau) = 0, \tag{4.10}$$

$$\delta\tau = \tau_{new} - \tau_{current} = -\frac{\delta\Phi}{\delta\tau}^{-1}\Phi(\tau_{current}), \tag{4.11}$$

$$\tau_{new} = \tau_{current} + \delta\tau. \tag{4.12}$$

The calculation of derivatives of tensors is defined here as:

$$\frac{d\mathbf{A}}{d\mathbf{B}} = \frac{d\mathbf{A}_{i,j}}{d\mathbf{B}_{l,k}} e_i \otimes e_j \otimes e_k \otimes e_l. \tag{4.13}$$

The partial derivative of the potential with respect to the equivalent stress can be derived straightforwardly:

$$\frac{\partial\Phi}{\partial\tau} = -\frac{\bar{\boldsymbol{\sigma}}^d : \bar{\boldsymbol{\sigma}}^d}{\tau^3} - \frac{\sqrt{3} f tr(\bar{\boldsymbol{\sigma}}^h)}{\tau^2}\sinh(\frac{\sqrt{3}}{2}\frac{\frac{1}{3}tr(\bar{\boldsymbol{\sigma}})}{\tau}). \tag{4.14}$$

The derivative used in $\dot{\Lambda}$, $\dfrac{\partial\Phi}{\partial\bar{\boldsymbol{\sigma}}}$ is less straightforward. The complete derivation is shown in Appendix A. The results is found as:

$$\frac{\partial\Phi}{\partial\bar{\boldsymbol{\sigma}}} = \frac{\bar{\boldsymbol{\sigma}}^d}{\tau^2} + \frac{f}{\sqrt{3}\tau}\mathbf{I}\sinh(\frac{\sqrt{3}}{2}\frac{\frac{1}{3}tr(\bar{\boldsymbol{\sigma}})}{\tau}). \tag{4.15}$$

In the model, the derivative $\dfrac{d\mathbf{F}}{d\mathbf{F}_e}$ is used to calculate the residual in the CI Newton-Raphson loop. This derivative changes due to the change in $\mathbf{D}_p$ or in this case also $\mathbf{L}_p$. The derivatives in the Newton-Raphson loop should be updated to ensure an optimal convergence. As $\mathbf{F}$ is composed of an elastic part $\mathbf{F}_e$ and a plastic part $\mathbf{F}_p$, this derivative can be split as:

$$\frac{d\mathbf{F}}{d\mathbf{F}_e} = \mathbf{F}_e \cdot \frac{\partial\mathbf{F}_p}{\partial\mathbf{F}_e} + \frac{\partial\mathbf{F}_e}{\partial\mathbf{F}_e} \cdot \mathbf{F}_p. \tag{4.16}$$

This can then be reduced to:

$$\frac{d\mathbf{F}}{d\mathbf{F}_e} =^4 \mathbf{I} \cdot \mathbf{F}_p + \mathbf{F}_e \cdot \frac{\partial \mathbf{F}_p}{\partial \mathbf{D}_p} : \frac{d\mathbf{D}_p}{d\bar{\boldsymbol{\sigma}}} : \frac{d\bar{\boldsymbol{\sigma}}}{d\mathbf{F}_e}. \tag{4.17}$$

With $^4\mathbf{I}$ the fourth order unit tensor. In the last term of Equation 4.17, $d\mathbf{D}_p/d\mathbf{F}_e$ is split as the derivative of the plastic deformation rate can be derived with respect to the stress. The derivative of the plastic deformation gradient with respect to the velocity tensor is already present in the model and calculated using an approximation, so does not have to be recalculated.
The easiest way to calculate $\frac{d\mathbf{D}_p}{d\bar{\boldsymbol{\sigma}}}$ is to split it into seperate parts, as was done by van Dommelen et al [2]. This gives partial derivatives to all variables in $\mathbf{D}_p$ dependent on the stress:

$$\frac{d\mathbf{D}_p}{d\bar{\boldsymbol{\sigma}}} = \frac{\partial \mathbf{D}_p}{\partial \bar{\boldsymbol{\sigma}}} + \frac{\partial \mathbf{D}_p}{\partial \tau}\frac{d\tau}{d\bar{\boldsymbol{\sigma}}} + \frac{\partial \mathbf{D}_p}{\partial \dot{\gamma}_p}\frac{d\dot{\gamma}_p}{d\bar{\boldsymbol{\sigma}}}. \tag{4.18}$$

The partial derivative of the plastic deformation rate to the stress can be calculated quite straightforward:

$$\frac{\partial \mathbf{D}_p}{\partial \bar{\boldsymbol{\sigma}}} = (1-f)\dot{\gamma}_p\tau\left[\frac{\partial \Phi}{\partial \bar{\boldsymbol{\sigma}}} \otimes \left(-(\bar{\boldsymbol{\sigma}} : \frac{\partial \Phi}{\partial \bar{\boldsymbol{\sigma}}})^{-1}(^4\mathbf{I} : \frac{\partial \Phi}{\partial \bar{\boldsymbol{\sigma}}} + \bar{\boldsymbol{\sigma}} : \frac{\partial^2 \Phi}{\partial \bar{\boldsymbol{\sigma}}^2})(\bar{\boldsymbol{\sigma}} : \frac{\partial \Phi}{\partial \bar{\boldsymbol{\sigma}}})^{-1}\right) + (\bar{\boldsymbol{\sigma}} : \frac{\partial \Phi}{\partial \bar{\boldsymbol{\sigma}}})^{-1}\frac{\partial^2 \Phi}{\partial \bar{\boldsymbol{\sigma}}^2}\right]. \tag{4.19}$$

The complete derivation can be found in Appendix A. This derivative requires yet another derivative, $\frac{\partial^2 \Phi}{\partial \bar{\boldsymbol{\sigma}}^2}$. This can be calculated by taking the derivative of the already calculated $\frac{\partial \Phi}{\partial \bar{\boldsymbol{\sigma}}}$ from Equation 4.15:

$$\frac{\partial^2 \Phi}{\partial \bar{\boldsymbol{\sigma}}^2} = \frac{1}{\tau^2}(^4\mathbf{I} - \frac{1}{3\tau}{}^4\mathbf{I}^*) + \frac{f}{6\tau^2}{}^4\mathbf{I}^* \cosh(\frac{\sqrt{3}}{2}\frac{\frac{1}{3}tr(\bar{\boldsymbol{\sigma}})}{\tau}), \tag{4.20}$$

with $^4\mathbf{I}^*$ defined as $\mathbf{I} \otimes \mathbf{I} = e_i \otimes e_i \otimes e_j \otimes e_j$. As described in equation 4.18 there are four remaining parts that need to be solved. $\frac{\partial \mathbf{D}_p}{\partial \tau}$ and $\frac{\partial \mathbf{D}_p}{\partial \dot{\gamma}_p}$ are straightforward to calculate. The calculation of the other two parts is explained here. To calculate $\frac{d\tau}{d\bar{\boldsymbol{\sigma}}}$ an additional derivative is introduced, $\frac{d\Phi}{d\bar{\boldsymbol{\sigma}}}$. Since Φ should remain 0, $\frac{d\Phi}{d\bar{\boldsymbol{\sigma}}}$ should also be 0. As was done before this derivative can be split into parts:

$$\frac{d\Phi}{d\bar{\boldsymbol{\sigma}}} = \frac{\partial \Phi}{\partial \tau}\frac{d\tau}{d\bar{\boldsymbol{\sigma}}} + \frac{\partial \Phi}{\partial \bar{\boldsymbol{\sigma}}} = \mathbf{0}. \tag{4.21}$$

As both partial derivatives were calculated in equations 4.14 and A.8, the needed derivative can be found as follows:

$$\frac{d\tau}{d\boldsymbol{\sigma}} = -(\frac{\partial \Phi}{\partial \tau})^{-1}\frac{\partial \Phi}{\partial \boldsymbol{\sigma}}. \tag{4.22}$$

This leaves one part to still determine. As the plastic strain-rate is dependent on the equivalent stress and the viscosity, which in turn are dependent on the stress, it can be split as was done previously:

$$\frac{d\dot{\gamma}_p}{d\bar{\boldsymbol{\sigma}}} = \frac{\partial \dot{\gamma}_p}{\partial \tau}\frac{d\tau}{d\bar{\boldsymbol{\sigma}}} + \frac{\partial \dot{\gamma}_p}{\partial \eta}\frac{d\eta}{d\bar{\boldsymbol{\sigma}}}. \tag{4.23}$$

As the viscosity η is defined as:

$$\eta = \eta_0 \frac{\frac{\tau}{\tau_0}}{\sinh(\tau/\tau_0)} \exp(\frac{\mu P}{\tau_0}) \exp(Sa \cdot R(\gamma_p)), \tag{4.24}$$

the derivative $\frac{d\eta}{d\bar{\boldsymbol{\sigma}}}$ can be split as:

$$\frac{d\eta}{d\boldsymbol{\sigma}} = \frac{\partial\eta}{\partial\tau}\frac{d\tau}{d\boldsymbol{\sigma}} + \frac{\partial\eta}{\partial P}\frac{dP}{d\boldsymbol{\sigma}} + \frac{\partial\eta}{\partial R}\frac{\partial R}{\partial\gamma_p}\frac{d\gamma_p}{d\boldsymbol{\sigma}}. \tag{4.25}$$

This leaves two derivatives which still needs to be determined. The first one is the derivative of the equivalent stress with respect to the elastic deformation gradient. This part can also be split as it is indirectly dependent on the elastic deformation, therefore leaving only one part to be determined:

$$\frac{d\tau}{d\mathbf{F}_e} = \frac{d\tau}{d\bar{\boldsymbol{\sigma}}} : \frac{d\bar{\boldsymbol{\sigma}}}{d\mathbf{F}_e}. \tag{4.26}$$

This leaves $\frac{d\bar{\boldsymbol{\sigma}}}{d\mathbf{F}_e}$ to be determined, which is also needed for the derivative of $\frac{d\mathbf{F}}{d\mathbf{F}_e}$ 4.17. The result is found as:

$$\frac{d\bar{\boldsymbol{\sigma}}}{d\mathbf{F}_e} = G_e((-\frac{2}{3}J_e^{-2/3}\cdot(\mathbf{F}_e^{-1})^T\cdot\mathbf{C}_e^d) + J_e^{-2/3}\frac{d\mathbf{C}_e}{d\mathbf{F}_e}({}^4\mathbf{I} - 1/3{}^4\mathbf{I}^*)) + \kappa\mathbf{I}(J_e\cdot(\mathbf{F}_e^{-1})^T). \tag{4.27}$$

4.1.2 Void Growth

To have a full void model growth should be incorporated. This can be done according to Gurson's void growth model [9]. During plastic deformation voids will start to grow. The original model of Gurson described this for incompressible material, so a constant volume. This gives the following equation [34]:

$$(1-f)\dot{V}_{matrix} - \dot{f}V_{matrix} = 0. \tag{4.28}$$

The volume change of the matrix, $\dot{V}_{matrix}$, can be defined as $tr(\mathbf{D}_p)V$. Then the growth in void volume fraction can be expressed as:

$$\dot{f} = (1-f)tr(\mathbf{D}_p). \tag{4.29}$$

This growth does not include direction of growth or coalescence. Also this model describes incompressible material, whereas this is not true in this case. Therefore, some form of dilatation compensation should be added. This is discussed in Section 4.1.4.
This void growth model describes void growth in existing voids. If there are no voids present in the material there will be no growth. To get a good void growth description void nucleation should therefore be taken into account.

4.1.3 Void Nucleation

Since there is no void fraction in a new sample, prior to deformation, voids should start to nucleate around the yield point. If no nucleation would be taken into account, a starting porosity should be present to show any growth. Therefore, an extension to the original Gurson model was used. This nucleation model was first proposed by Needleman and Rice [22]. They proposed a stress controlled nucleation. Chu and Needleman [23] proposed a strain-controlled nucleation. As can be seen in Figure 4.3a, regardless of temperature, the nucleation will occur around the same strain. While the yield point changes due to strain-rate, see Figure 4.3b, the model parameters have to be changed only once per strain-rate. For the stress controlled nucleation this has to be done for every temperature as well as every strain-rate. Therefore the strain controlled model was used.

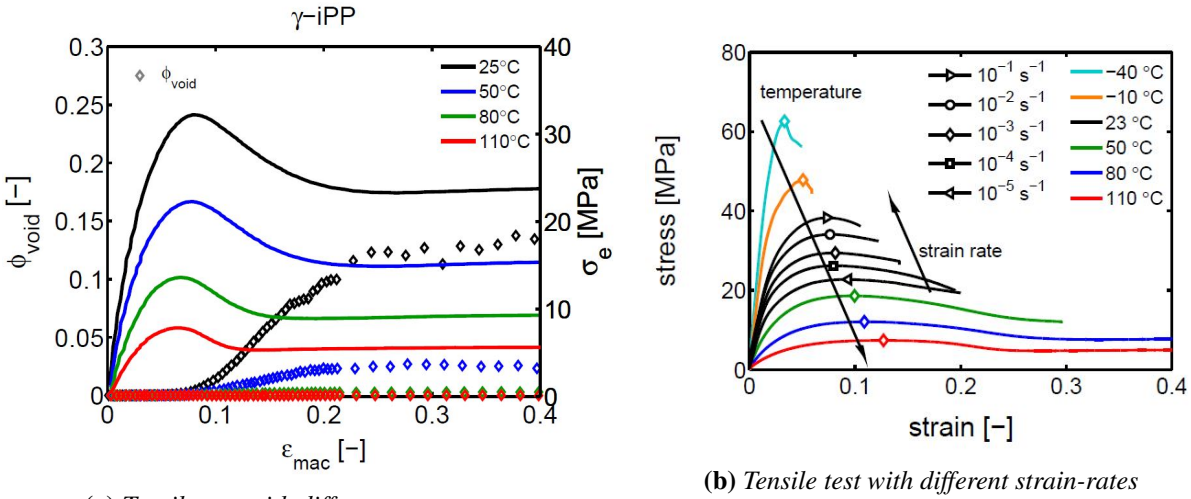

(a) *Tensile test with different temperatures*

(b) *Tensile test with different strain-rates*

Figure 4.3: *The results found by Caelers [7]*

As can be seen in Figure 4.3a the voids for $\alpha - iPP$ start to grow just before the yield point. The model presented by Needleman and Chu was based on a standard distribution. The nucleation term was simply added to the growth resulting in the following porosity evolution:

$$\dot{f} = \dot{f}_{grow} + \dot{f}_{nucl}, \tag{4.30}$$

$\dot{f}_{grow}$ being the growth described previously, and $\dot{f}_{nucl}$ was defined as the nucleation contribution:

$$\dot{f}_{nucleation} = \dot{\bar{\gamma}}_p \frac{\phi}{s\sqrt{2\pi}} \exp(-\frac{1}{2}(\frac{\bar{\gamma}_p - \gamma_N}{s})^2), \tag{4.31}$$

with ϕ being the fraction of nucleating material. γ_N is the strain at which half of the voids has nucleated. s is the standard deviation, defining the strain span over which these voids will nucleate.
It should be noted that the nucleation is limited to tension via the condition that tr($\mathbf{D}_p$)>0. If the trace is negative this would note compression of the material and when zero there is a stress free state, where no nucleation is present.

4.1.4 Dilatational Compensation

As was discussed in Section 4.1.2, the Gurson model assumes incompressible matrix material around the voids. This is not true. As the material deforms there will also be an elastic contribution. Therefore the voids will grow more than they in reality do as the volume of the matrix is not constant. To compensate for this, the total void fraction is recalculated after every increment.
The void fraction (Equation 4.1) can be written as follows:

$$f = \frac{V_{void}}{J_e V_{m,0} + V_{void}}, \tag{4.32}$$

with $V_{m,0}$ the initial matrix volume. This can be rewritten:

$$\frac{1}{f} = J_e \frac{V_{m,0} + V_{void}}{V_{void}} - J_e + 1. \tag{4.33}$$

The void volume fraction not accounting for volume change can then be defined as:

$$f_0 = \frac{V_{void}}{V_m + V_{void}}. \tag{4.34}$$

This results in the following actual void fraction:

$$f_{actual} = \frac{f_0}{J_e - J_e f_0 + f_0}, \tag{4.35}$$

with f_0 being the uncompensated void fraction and $J_e = det(F_e)$ the elastic volume change ratio.

4.1.5 The extended modified yield surface

To increase the accuracy of the Gurson model, numerous extensions have been made. One of these extensions was made by Tvergaard and Needleman [11]. This extension is widely used. The extension is a phenomenological model, rather than a micro-mechanical model like the original Gurson model. However, this model allows an increased porosity and hydrostatic influence on the response. This is done by introducing two variables, q_1 and q_2. These are introduced in the potential:

$$\Phi = \frac{1}{2}\frac{\bar{\boldsymbol{\sigma}}^d : \bar{\boldsymbol{\sigma}}^d}{\tau^2} + 2fq_1 \cosh(\frac{\sqrt{3}}{2}q_2\frac{\frac{1}{3}tr(\bar{\boldsymbol{\sigma}})}{\tau}) - (1 - (fq_1)^2) = 0. \tag{4.36}$$

If there is a porosity and q_1 and q_2 are larger than 1, the yield surface will decrease, resulting in a shift in the stress-strain response. As can be seen in Equation 4.36, q_1 has an influence on the effect of the porosity. With increasing q_1 the porosity will have an increased effect on the potential. Similarly there can be seen that q_2 will affect the hydrostatic stress influence on the potential. These variables can be tuned to experimental results to give a better material response.

5 Results

The previously proposed Gurson model was first implemented in a purely EGP framework to see the influence of the different parameters. These results are used to see the trends of the model including voiding. Afterwards the model is used in the Composite Inclusion Model itself. These results are compared to experimental results obtained by Caelers et al. [7] with experiments on isotactic-Polypropylene.

5.1 Purely EGP Model

A purely glassy polymer framework was first used to check the Gurson model. This was done using a material description with a single mechanism and a single mode. This is therefore merely to see the influence of certain parameters included in the Gurson model.

5.1.1 Gurson Potential influence

First the standard Gurson model was implemented. This model does not include void growth or nucleation yet. To see the influence of the model a starting porosity was therefore introduced. The model was implemented as was described in Section 4. This EGP framework is similar to the CIM but does not include the crystalline part.
As was stated this model uses a single mode, single mechanism description. While a multi mode model would show a better approximation prior to yield, this should not influence the results of voiding significantly as this occurs at or slightly before the yield point. The use of a single mode description can easily be seen in the results due to the nearly linear stress-strain response before the yield point. While a multi mode description would be preferential, this posed a problem due to the added hydrostatic stress influence. Since the plastic deformation rate now includes hydrostatic stress, the volumetric change should be included in the stress for all modes. The original formulation used the volumetric change of the first mode only, making use of an overall pressure. To include this, a pressure should be defined for every mode. Currently, however, the CIM for a multi mode model uses a deformation gradient calculated in the previous increment per mode. In the next increment, the new viscosity is calculated and used to define the new deformation gradient. By adding a hydrostatic dependence, the volumetric change should be included in the viscosity per mode. To calculate the volumetric change, $J_e = det(F_e)$, the new deformation gradient is needed, while only the deformation gradient of the previous increment is present. Since resolving this problem would be too time consuming and not needed at this stage, the single mode model was used. The parameters used in the purely EGP model are given in table 5.1, with the aging parameters shown in table 5.2.

η_0 [MPa s]	G [MPa]	G_r [MPa]	κ [GPa]	ΔU [kJ/mol]	V_{act}	T_{ref} [$^\circ K$]	μ
4.8861*10^{15}	324	1.2	1.66	2.74*10^5	3.35*10^{-27}	296.15	0.017

Table 5.1

S_a	r_0	r_1	r_2
5.2	0.955	2	-1

Table 5.2

To see what the influence was of the Gurson model on the stress-strain response multiple initial porosities were used. These results are shown in Figure 5.1. This Figure shows the results for a tensile test at 23°C and a strain-rate of 10^{-2} s^{-1}. It shows an expected result of a downward shift of the stress-strain curve. This downward shift can be logically explained by the fact that with a porosity present in the material there

will be less material to cope with the stress. This can also be seen through the potential (Equation 4.2). As the porosity increases the equivalent stress will increase through the Newton-Raphson calculations to keep the potential at zero.

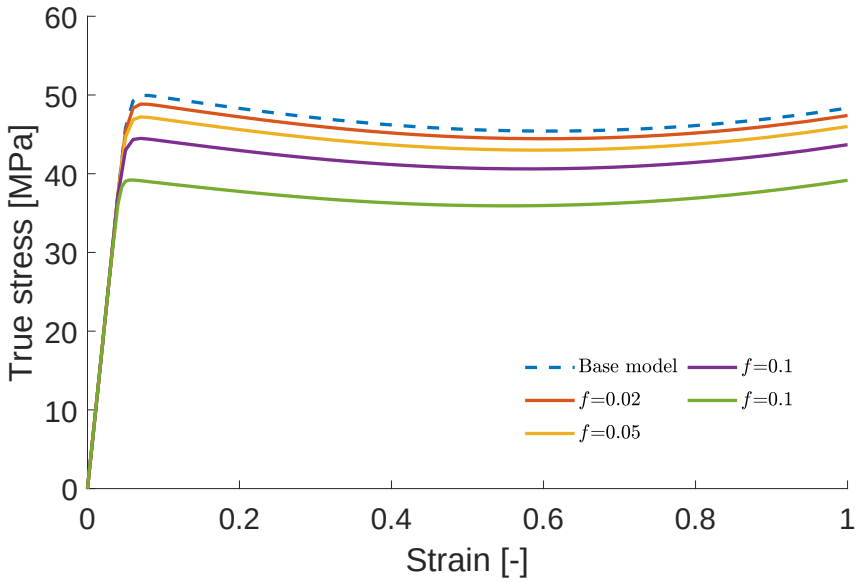

Figure 5.1: *The purely EGP results, true stress, including a constant porosity, tension case for 23°C, strain-rate* $10^{-2}\ s^{-1}$.

5.1.2 Growth

The next step is to implement the growth of voids in the model. As stated in Section 4.1.2 a porosity should be present for the Gurson growth model to show any growth. Therefore three cases were considered. One with a porosity of zero, a 2% porosity and a 10% porosity. The porosity evolution is included to see the behaviour of the model. The results shown in Figure 5.2 were simulated using again a 23°C temperature and a 10^{-2} s^{-1} strain-rate.

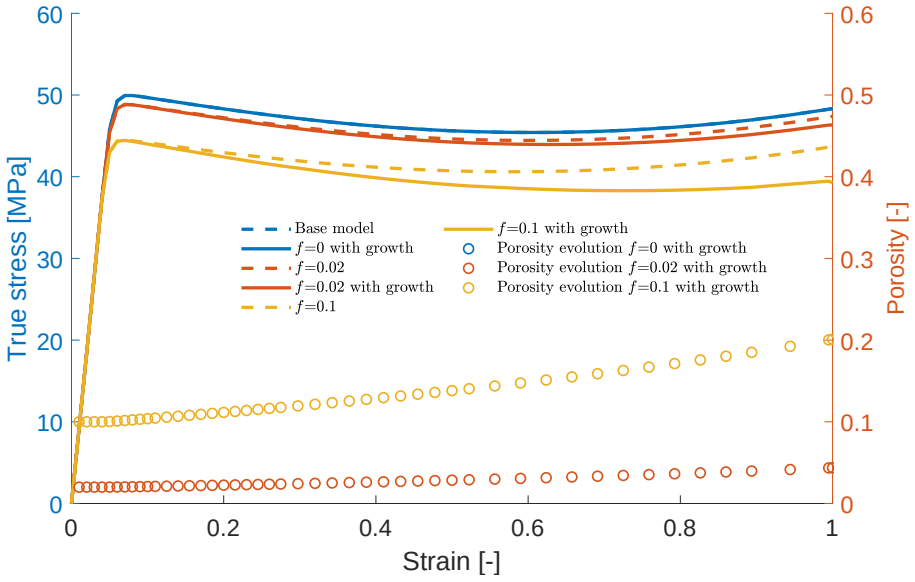

Figure 5.2: *The purely EGP results, true stress, including growth, tension case for 23°C, strain-rate* $10^{-2}\ s^{-1}$.

To get a clear view on the growth impact the model without growth but with a constant porosity is also included for all three cases. As can be seen the results of the zero initial porosity case is equal for both the non growth model and the growth model. This should be expected as there should be no growth without existing voids due to tr($\mathbf{D}_p$) being 0 for the Gurson model to be incompressible.
For the other cases, it can be seen that the growth in porosity causes a decrease in the stress response. It can also be noted that a larger starting porosity will have an increased effect on the growth response. This can be expected since the volume of voids that can grow is larger, than with a smaller initial porosity.
An increased softening of the material can also be observed after yielding, due to the increased void size. While the increase of softening is rather small, this effect should be enhanced by including nucleation, which can result in a higher porosity.
The effect of this growth model can also be checked in a compression test. When in compression there should be a decrease in porosity, caused by the shrinking and collapsing of the voids due to the pressure. Using the same temperature and strain-rate of 23°C and 10^{-2} s^{-1} respectively the results displayed in Figure 5.3 were obtained:

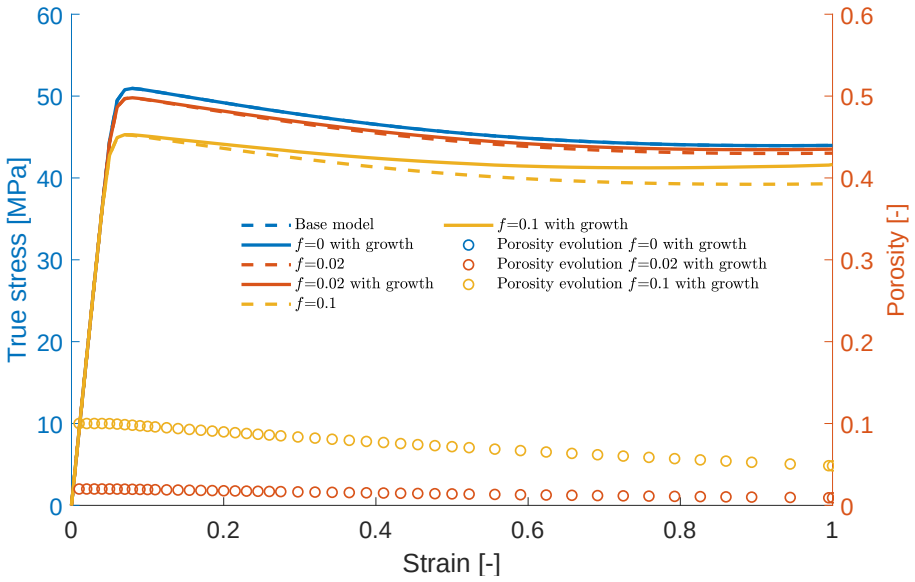

Figure 5.3: *The purely EGP results, true stress, including growth, compression case for 23°C, strain-rate* 10^{-2} s^{-1}.

The shrinkage in void volume fraction can be seen as well as a simultaneous increase in stress. As can be seen this porosity will reduce to zero. At a porosity of zero there are no voids able to shrink, automatically limiting the porosity to zero.

5.1.3 Nucleation

To get the increase in void fraction without an initial porosity nucleation should be added. This was done with a strain controlled nucleation, as discussed in Section 4.1.3. The parameters of this model can be tuned to increase the speed of nucleation and the amount of nucleating voids. Using the same simulation conditions as described before, the results as shown in Figure 5.4a were obtained.

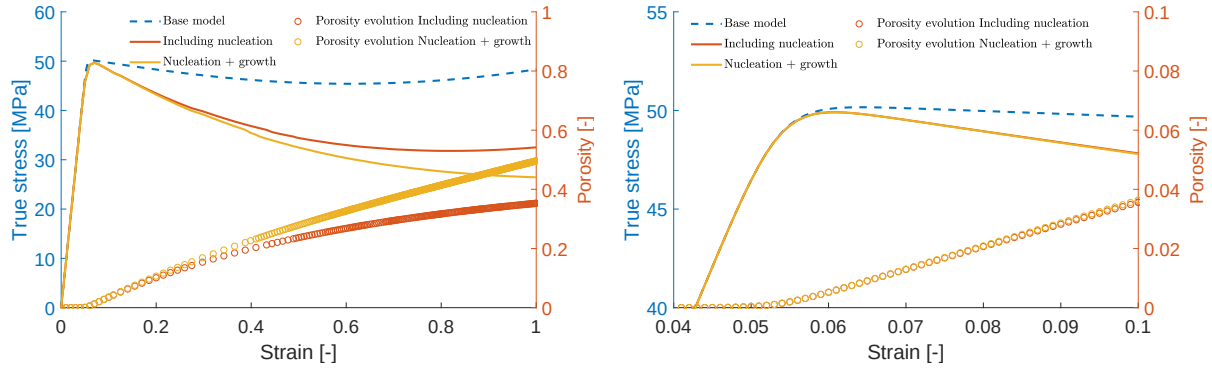

(a) *The results with a large strain.* **(b)** *The results around the yield point.*

Figure 5.4: *The purely EGP results, true stress, including nucleation, tension case for 23°C, strain-rate* $10^{-2}\ s^{-1}$.

It can be seen that voids start to appear in the model when there is plastic deformation. This is shown in Figure 5.4b more clearly. This is in-line with the experimental observations of Caelers which showed voids at yielding. Around the yield point, there is little difference between the model containing only nucleation and the model containing only growth. This is due to the small porosity, showing little growth. When looking at larger strains, a clear difference can be observed between the models. As can be seen in the experimental results shown in Figure 2.8, the hardening after yield is negated by the void growth. This effect can also be seen in Figure 5.4a. It can also be seen that the void evolution levels off, similar to experimental results found by Caelers et al. Whether this is due to the voids being undetectably large or collapsing of the voids is rather important in the argument whether the levelling off is correct and should be looked into. From the results found by Caelers et al., an increased softening was also observed between compression and tension. While the addition of void growth shows increased softening, this effect can be further enhanced by adding nucleation. This also shows in the results of Figures 5.5a and 5.5b, where the nucleation parameters show a large influence on the post yield behaviour.
The nucleation model introduces two parameters which can be fitted to experimental results. As was discussed in Section 4.1.3, these are the standard deviation and the nucleation strain where half of the total nucleation has occurred. Increasing the standard deviation should allow for the adjustment of the slope of the nucleation around the nucleation strain. The nucleation strain can be used to shift the point of nucleation.

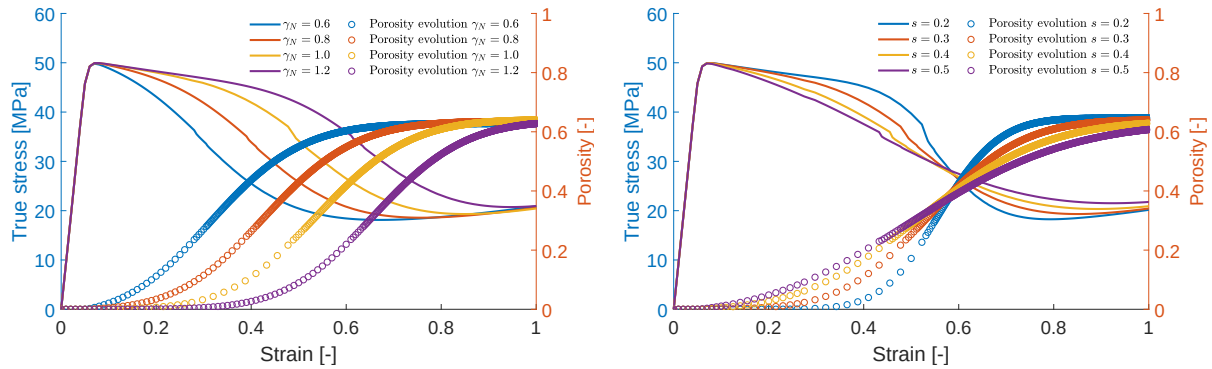

(a) *The influence of* γ_N *on the nucleation of voids, s=0.3.* **(b)** *The influence of s on the nucleation of voids,* γ_N*=1.0.*

Figure 5.5: *The results for different nucleation parameters, 23°C, strain-rate* $10^{-2}\ s^{-1}$.

As can be seen in Figures 5.5a and 5.5b the standard deviation indeed changes the slope of the nucleation. From Figure 5.5a it can be seen that γ_N indeed shifts the nucleation point while keeping the same slope in

the function, as would be expected from the normal distribution it is based on. Figure 5.5b also shows the increase of the nucleation span with increasing s, while keeping the total void fraction at γ_N equal. These parameters can be tuned to experimental results to show the right voiding response of the material.

5.1.4 Dilatation

The dilatation compensation described in Section 4.1.4 should decrease the porosity when applying a tensile stress due to the elastic stretching of the matrix. The results for a cases with and without the adjusted porosity are shown in Figure 5.6. This is done using a strain-rate of 10^{-2} for 23°C.

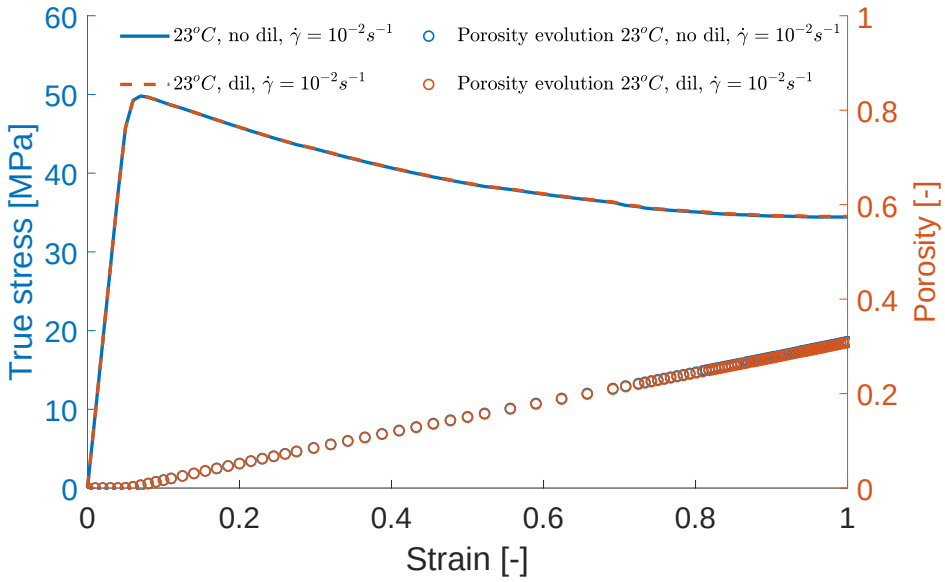

Figure 5.6: *The results of the EGP model including and excluding dilatation compensation, for 23°C, strain rate $\dot{\gamma}$ 10^{-2}.*

As can be seen in the Figure the dilatation is very small in the purely EGP model. This is due to the high elastic resistance of the purely amorphous material. The influence of elasticity will be much larger when incorporating the crystalline phase, as in the CIM the elastic resistance of the amorphous phase is lower.

5.1.5 Extension Tvergaard & Needleman

As was discussed in Section 4.1.5 the two variables introduced by Tvergaard and Needleman increase the porosity influence and the hydrostatic stress influence. These relations can also be seen in Figures 5.7a and 5.7b, with the influence of parameter q_1 and the second of q_2 respectively. From these Figures there can be concluded that the parameters show the desired effects. q_1 increases the porosity influence, leading to a difference in yield surface, hence the decrease in stress for increasing values.
q_2 shows an increased porosity at increasing strains. Due to the increased hydrostatic stress dependence the porosity will rise, as this drives the porosity. These parameters can be used to tune the results to experimental values.

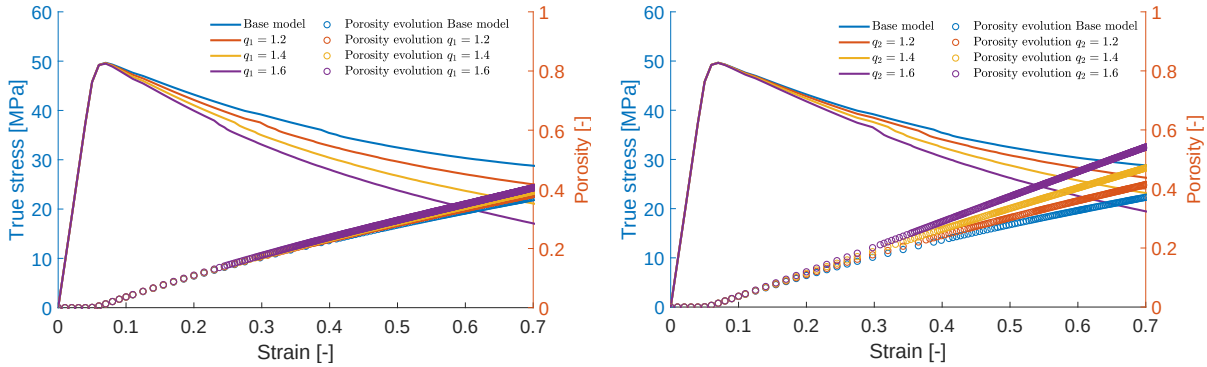

(a) *The influence of the introduced parameter q_1.* **(b)** *The influence of the introduced parameter q_2.*

Figure 5.7: *The results for the EGP model for different q_1 and q_2.*

5.1.6 Temperature and strain-rate influence

Several experimental studies [6,7,32,33,37] have shown that the amount of voiding under tension is related to the conditions of the experiment. In these experiments the strain-rate and temperature were found to influence the voiding of the polymer. With increasing temperature there was less voiding showing. With increasing strain-rate the voiding increased. In Figure 5.8a the model for 23°C and 73°C are shown. The strain-rates for both cases are 10^{-2} and 10^{-3}.

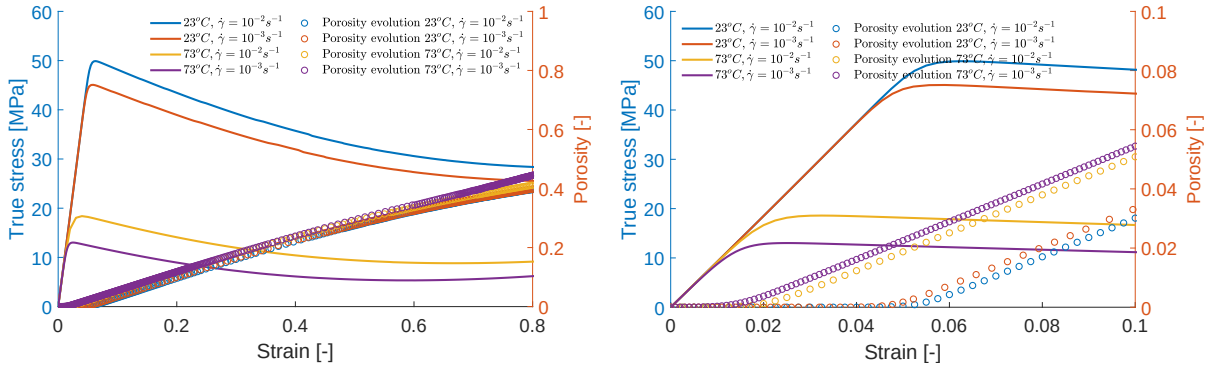

(a) *The influence of temperature and strain-rate for the EGP model, including voiding and growth.* **(b)** *The influence of temperature and strain-rate for the EGP model, around the yield point.*

Figure 5.8: *The results for the EGP model for different strain rates and temperatures.*

For all cases the same nucleation parameters were used, $\gamma_N = 0.5$ and $s = 1$. As can be seen the resulting porosities are quite similar. This shows a very small influence of strain-rate and temperature on the porosity. When looking closer around the yield point, see Figure 5.8b, there can however be seen that the void nucleation starts around the yield point, which is at a lower strain for lower temperatures and lower strain rates. The slopes for the porosity evolution, however, are similar, while a difference was observed in the experimental results from Caelers et al [7] for different temperatures. This could note that the nucleation parameters do have to be changed according to the test case, whereas in Section 4.1.3 the assumption was made that only one set was needed.

5.2 Composite Inclusion Model

The purely EGP Gurson model can be implemented in the CI pretty straightforward as the CI uses an EGP model for the amorphous phase description. The parameters used in this case remain single mechanism, single mode descriptions for the EGP model. The crystalline phase features a multi mechanism model. Due to the single mechanism, single mode EGP model different material parameters have to be used, depending on the temperature.

5.2.1 Gurson Potential influence

In the CI model the same model as described for the purely EGP phase was used. Therefore first the model was implemented using a constant porosity, to see the influence on the complete material response. These results are shown in Figure 5.10. Since Caelers et al. did tensile bar measurements the results that were found can not be used to verify the results found using the Gurson model, as discussed in Section 2.3. The trends of the model should represent the results found by Caelers et al., but the stress found in the experiments will be lower than the stress in the middle of the sample, where the porosity is measured. Therefore at the same stress the model will show less void growth. As the porosity in Caelers' measurement did not show a significant value for α i-PP above 23°C these higher temperature porosities are not displayed. Since the results from Caelers et al. will differ from the CIM results, only the trends of Caelers' findings can be used for comparison. The results shown in Figure 5.10 are in engineering stress and strain, as the results obtained by Caelers et al. were in these terms.
For the implementation in the CIM the same orientation distribution was used for all separate implementation, so a good comparison can be made. This distribution for all principal directions is shown in Figure 5.9. The parameters used in the simulations of the EGP part of the CIM are given in table 5.3. In the test cases 100 inclusions were used with a 60% crystallinity. The aging parameters are given in table 5.4.

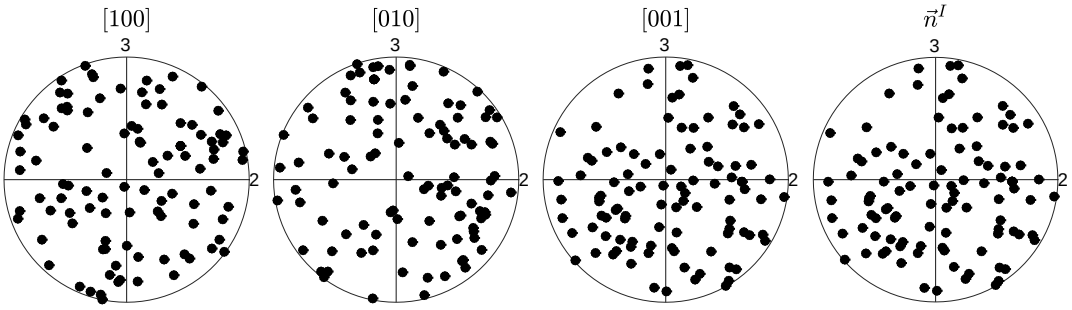

Figure 5.9: *The initial orientation used in the CIM for all test cases, 100 inclusions.*

η_0 [MPa s]	G [MPa]	G_r [MPa]	κ [GPa]	ΔU [kJ/mol]	V_{act}	T_{ref} [$^\circ K$]	μ
5.6*10^{13}	70	0.6	1.1	10^5	3.25*10^{-27}	296.15	0

Table 5.3

S_a	r_0	r_1	r_2
8	0.95	2	-3

Table 5.4

The elastic parameters for the crystalline phase are from Tashiro et al [48]. The rest of the parameters needed for the crystalline phase are given in table 5.5.

Slip system	$\dot{\gamma}_{0,T_{ref}}$ [s^{-1}]	V_{act}	ΔU [kJ/mol]	μ [-]
(010)[001]	0.4212*10^{-5}	2.8*10^{-27}	2.8*10^{5}	0.05
(100)[001]	0.0611*10^{-5}	3.08*10^{-27}	2.5*10^{5}	0.15
(110)[001]	0.0035*10^{-5}	4.2*10^{-27}	2.3*10^{5}	0.15
(1-10)[001]	0.0035*10^{-5}	4.2*10^{-27}	2.3*10^{5}	0.15
(010)[100]	0.0122*10^{-5}	3.36*10^{-27}	2.3*10^{5}	0.15
(100)[010]	0.0012*10^{-5}	3.36*10^{-27}	2.3*10^{5}	0.15
(110)[1-10]	0.0035*10^{-5}	4.2*10^{-27}	2.3*10^{5}	0.15
(1-10)[110]	0.0035*10^{-5}	4.2*10^{-27}	2.3*10^{5}	0.15

Table 5.5

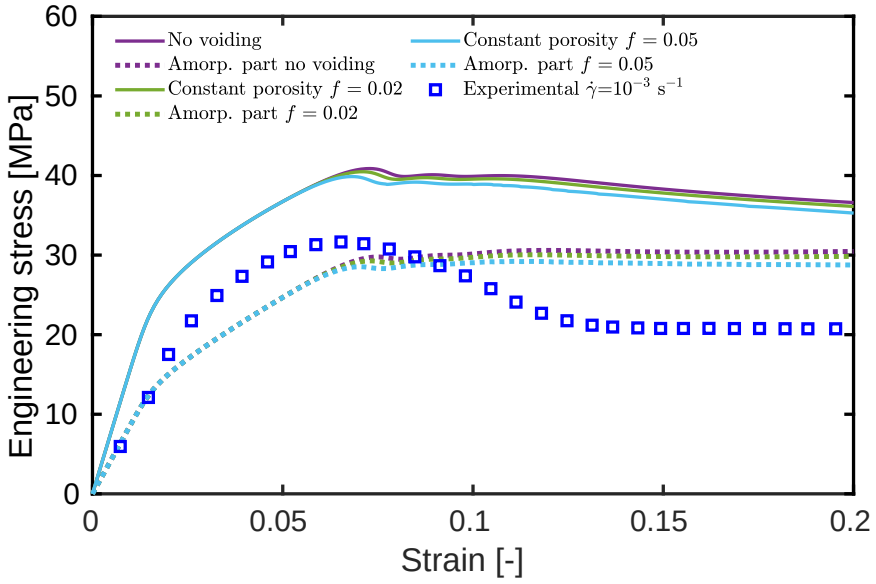

Figure 5.10: *The Composite Inclusion model results with a constant porosity, 23°C, strain-rate of* 10^{-3} s^{-1}.

In the figure, it can be seen that a constant porosity has a similar effect on the stress-strain response as was seen in the amorphous model 5.1.1. The porosities of the models are defined in the amorphous phase. In the figure, the volume averaged porosity is shown and as the crystallinity is approximately 60%, this value is significantly lower than in the amorphous phase itself. This volume averaged porosity, here noted as f_{void} for clarity, is calculated as:

$$\bar{f}_{void} = \frac{1}{N}\sum_{i=1}^{N}(f^a f_{void}). \tag{5.1}$$

The experimental porosity shown in the Figure are the porosity results from Caelers et al. for α i-PP at 23°C with a strain-rate of 10^{-3} s^{-1}. The experimental stress-strain curve is a tension measurement from Caelers et al. at 23°C.
Additionally, the absolute normalised average strain-rate of the crystalline slip systems and the amorphous can be plotted. In Figure 5.11, the active slip systems can be seen for the case without voiding. It shows a large increase of amorphous strain-rate at the yield point and the most active slip system, (010)[100].

The dips in the stress-strain results from the model are caused by the sudden activation of slip systems. Simultaneously to the slip system activation a strain-rate increase in the amorphous phase is caused, also showing in Figure 5.11. These peaks are also present in the model without the Gurson implementation. The peaks show at the same strain as the yield point, where the stress decreases. For reference these results are also plotted in engineering strain.

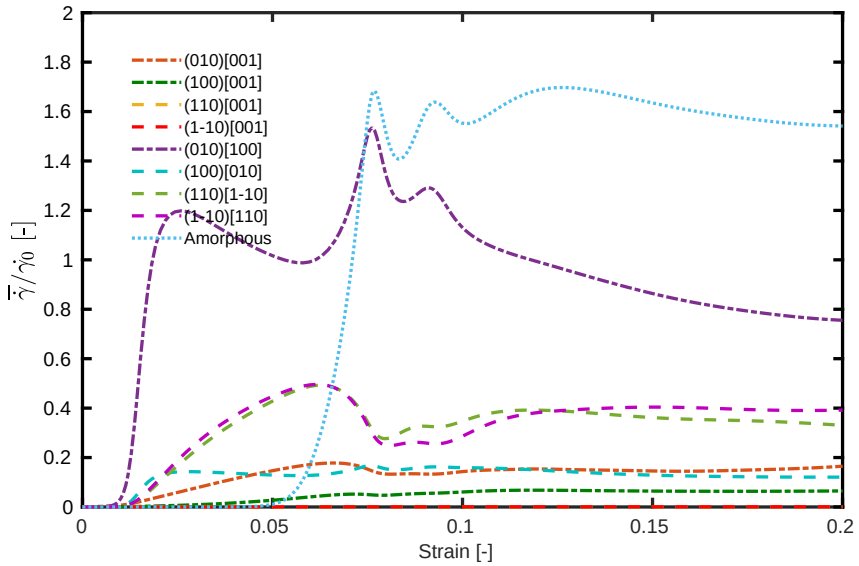

Figure 5.11: *The absolute normalised average strain-rate vs. the engineering strain for a no voiding case, 23°C, strain-rate of* $10^{-3}\ s^{-1}$.

To get a microscopic picture of the results, pole figures were used. In Figure 5.12 the strain-rate per inclusion is shown with its orientation of the interface normal, chain direction of the crystals and transverse directions. The pole figures are taken at a strain of 0.2, which is after yielding. The results for 100 inclusions, without and with a porosity of 0.02 are shown in Figures 5.12 and Figure 5.13 respectively. As can be seen the interface normals of the inclusions showing the largest deformation are oriented nearly perpendicular to the tensile axis. Since the chain direction of the crystals is nearly perpendicular to the interface these are also oriented the same way as the interface normals. At larger strains they will start to diverge. When plotting the strain-rate, it can be seen that the inclusions showing very large deformations are oriented similarly.

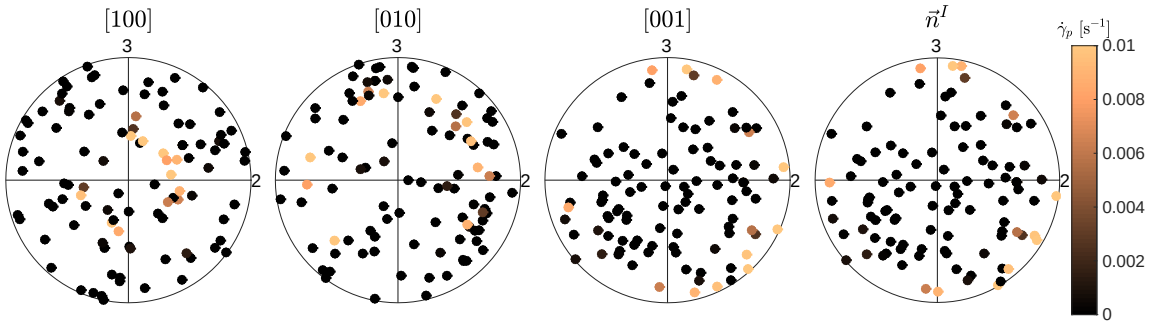

Figure 5.12: *Pole figures for the no voiding case with from left to right: [100], [010], [001] and interface normal directions. The colour indicates the absolute strain-rate in the amorphous phase.*

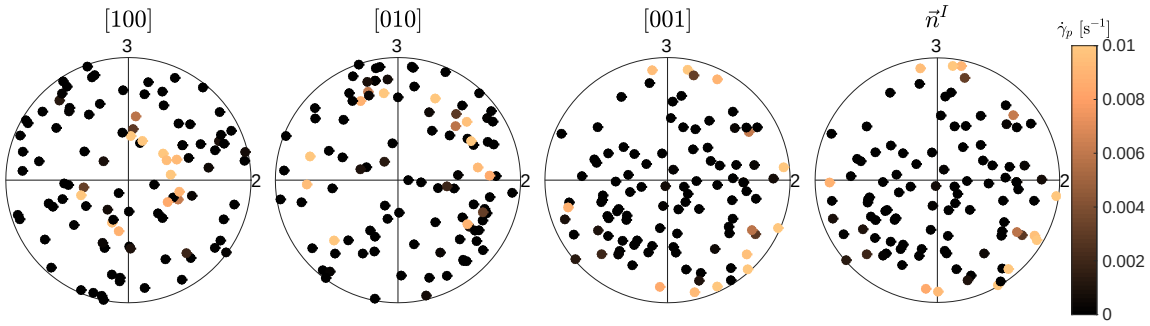

Figure 5.13: *Pole figures for the $f = 0.02$ case with from left to right: [100], [010], [001] and interface normal directions. The colour indicates the absolute strain-rate in the amorphous phase.*

Overall the two cases show very similar results, which would be expected as the porosity is constant. This can also be seen by looking at the most active slip system, (010)[100], for which pole figures indicating the strain-rate of the (010)[100] slip system are shown in Figures 5.14 and 5.15. The same inclusions are active in this slip system.

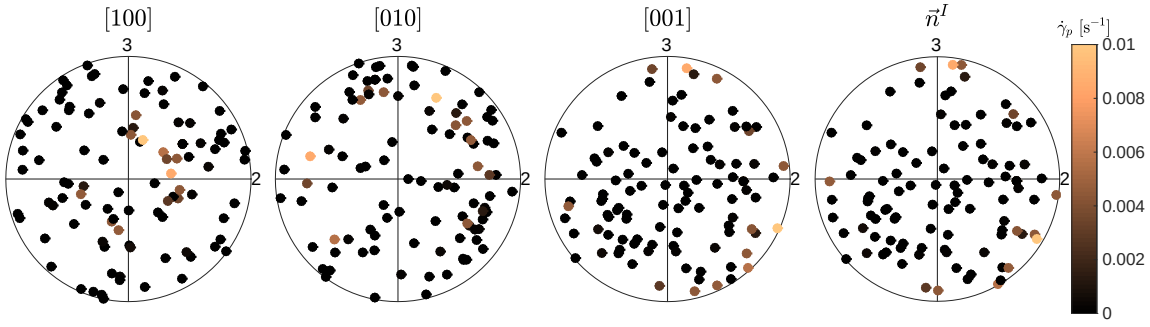

Figure 5.14: *Pole figures for the case without voids, with from left to right: [100], [010], [001] and interface normal directions. The colour indicates the absolute shear-rate in the most active slipsystem (010)[100].*

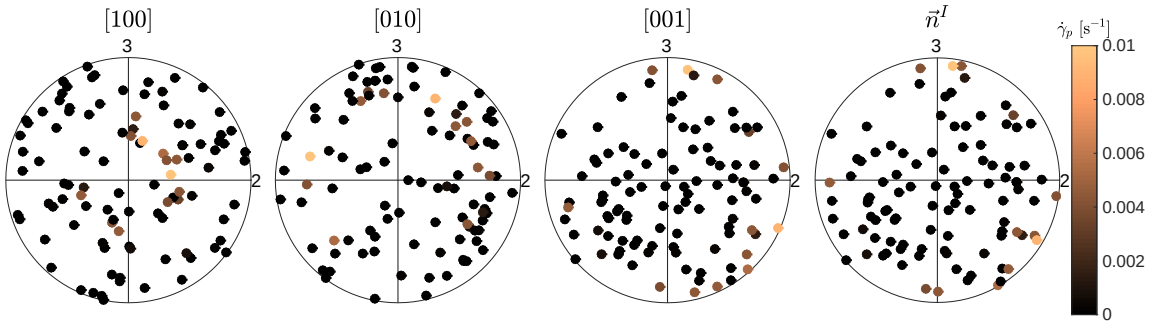

Figure 5.15: *Pole figures for the $f = 0.02$ case with from left to right: [100], [010], [001] and interface normal directions. The colour indicates the absolute shear-rate in the most active slipsystem (010)[100].*

5.2.2 Growth

Growth was incorporated in the same manner as described for the pure EGP model, see Section 4.1.2. Like discussed a porosity has to be present to see any growth in the model. Therefore a small porosity was chosen at $f = 0.02$ of the amorphous phase. Similarly as the constant porosity here a temperature of 23°C was used, with a strain-rate of 10^{-3} s^{-1}. The results from Caelers et al. will be shown as reference. At an engineering strain of 0.15 for these conditions, there is a sudden increase in void volume, showing in merely one inclusion. This increase is so significant that the void fraction becomes too big, resulting in failure of the model. This increase is caused by the peaks in strain-rate response as was shown for the constant porosity case. These peaks show in the same inclusion that show these large growths. As the growth is linked to the trace of the plastic deformation rate this gives rise to large growths. This problem clearly shows in Figure 5.17. The normalised strain-rate goes to enormous values due to the blowing up of an inclusion. The inclusions that are blowing up and displaying a large void fraction are the inclusions that already show very large deformations without void growth, or even voids at all. This can be seen in the pole figures in Figure 5.18.

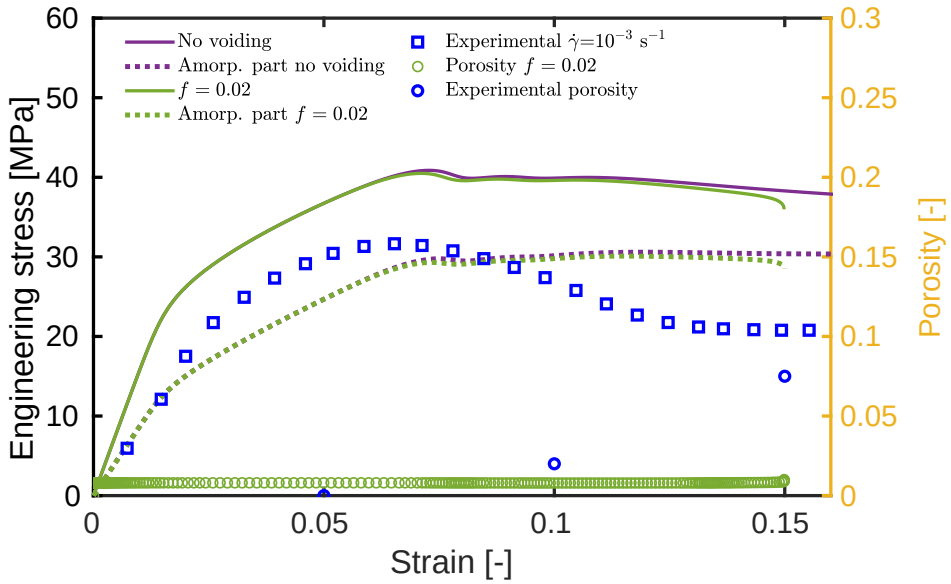

Figure 5.16: *The Composite Inclusion model stress-strain response with void growth, 23°C, strain-rate $10^-3\ s^{-1}$.*

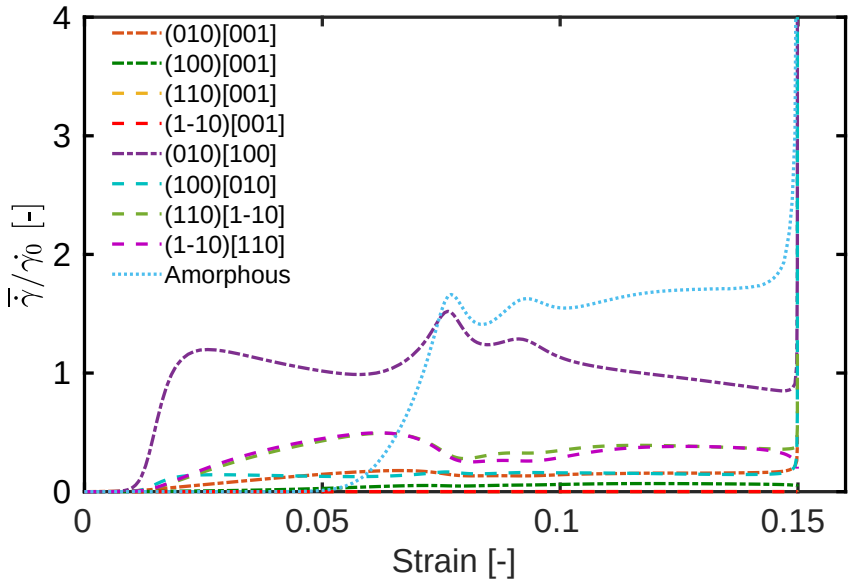

Figure 5.17: *The absolute normalised strain-rate vs. the strain for void growth with a starting porosity of 0.02, 23°C, strain-rate* $10^{-}3\ s^{-1}$.

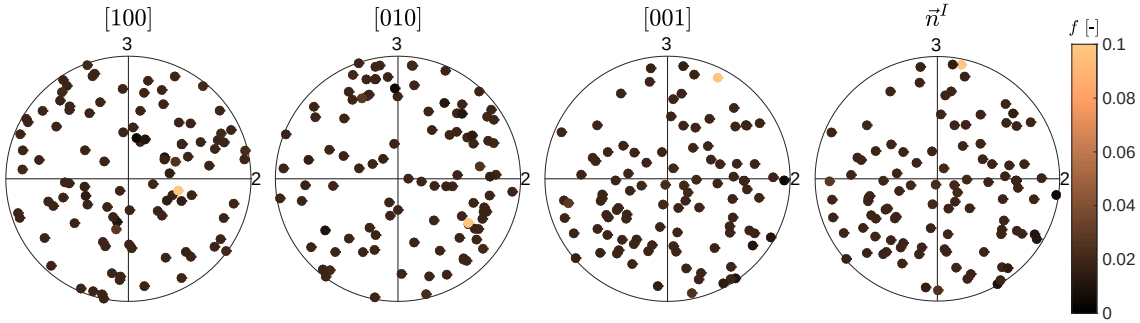

Figure 5.18: *Pole figures for the case including growth, starting porosity* $f = 0.02$*, with from left to right: [100], [010], [001] and interface normal directions. The colour indicates the porosity in the amorphous phase.*

As shown in Figure 5.18 the porosity is concentrated in one inclusion. The colour spectrum was set to a maximum of 0.1 to show the large difference to the rest, while in reality the porosity of this inclusions amorphous phase exceeded 0.55. One thing that stands out is the fact that this inclusion is not the inclusion showing the largest plastic strain-rate without growth, see Figure 5.12.

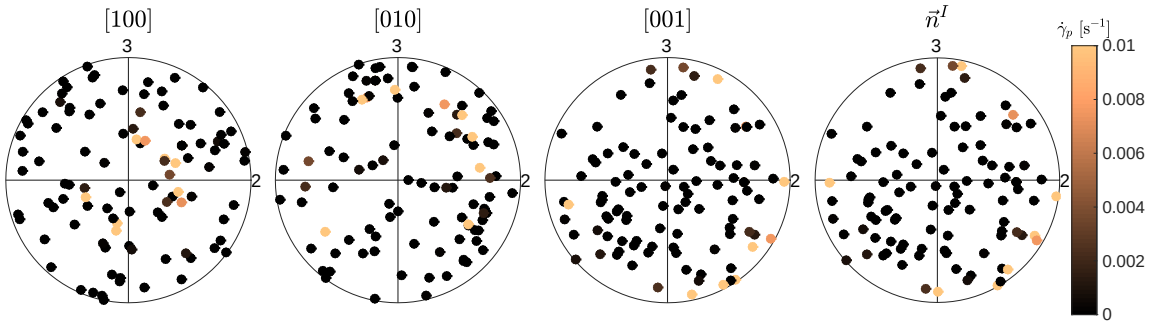

Figure 5.19: *Pole figures for the case including growth, starting porosity $f = 0.02$, with from left to right: [100], [010], [001] and interface normal directions. The colour indicates the absolute strain-rate in the amorphous phase.*

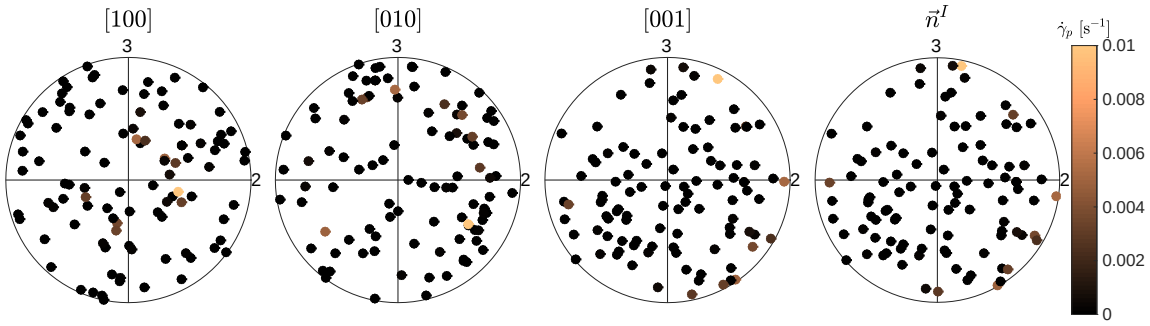

Figure 5.20: *Pole figures for the case including growth, starting porosity $f = 0.02$, with from left to right: [100], [010], [001] and interface normal directions. The colour indicates the absolute shear-rate in the most active slipsystem (010)[100].*

Looking at Figures 5.19 and 5.20 it can be seen that the amorphous phase shows similar strain-rates as the non growth model, Figures 5.12 and 5.13. The strain-rate in slip system (010)[100] however shows fewer high strain-rate inclusions, see Figure 5.14.
This problem was tried to resolve using a hydrostatic hardening. This hardening would result from the hardening of the material around the void, due to the stretching of the chains around the void. Unfortunately this did not have a significant effect as the strain-rate in certain voids was simply too high. This hydrostatic hardening was defined using the volumetric change of the amorphous phase, instead of the elastic volumetric change, as defined in the hardening stress. This was done as the void influence was included in the plastic deformation rate to stop the "blowing up of an inclusion". This resulted in the following hardening equation:

$$\boldsymbol{\sigma}_r = G_r(J_e^{-2/3})\mathbf{B}_r^d + \kappa_a \frac{G_r}{G_e}(J_e - 1)\mathbf{I}, \tag{5.2}$$

with $\mathbf{F}$ the complete deformation gradient. The factor $\dfrac{G_r}{G_e}$ was added to keep the balance between the hardening and driving stress. J_e is defined as the elastic volumetric change $det(\mathbf{F}_e)$. As the assumption in the model was made that the volumetric change is completely elastic, J_e defines the complete volumetric change.
Another way to solve this problem could be to limit the strain-rate of the inclusion. This can be done

by setting a maximum value for $\dot{\gamma}_p$ and letting the equivalent stress increase. The best way to do this would be to have smooth transition between the current formulation of the plastic strain-rate, τ/η, and the limit. When limiting the strain-rate the deformation will be more equally distributed over the inclusions. It should also limit the growth from massively increasing due to enormous strain-rates. When doing this the derivatives in Equation 4.23 will also have to change, according to the new function. While this is a rather un-physical solution it should allow for proper void growth and reduces the large differences between similar oriented inclusions. This can be done by using an activation function, like a hyperbolic tangent. This function will have to be scaled between 0 and 1 and should activate the maximum value and deactivate the normal plastic strain-rate description. To keep the strain-rate profile as close to reality as possible the activation should be set close to the maximum. However, due to the time spectrum of this project, this could not yet be completed.

5.2.3 Nucleation

As the implementation of the growth mechanism posed some problems, here the nucleation implementation is shown excluding growth. The same case was used as before, 23°C and a strain-rate of 10^{-3} s^{-1}. To show the influence of the nucleation parameters γ_N and s, these are varied. These results are shown in Figure 5.21.

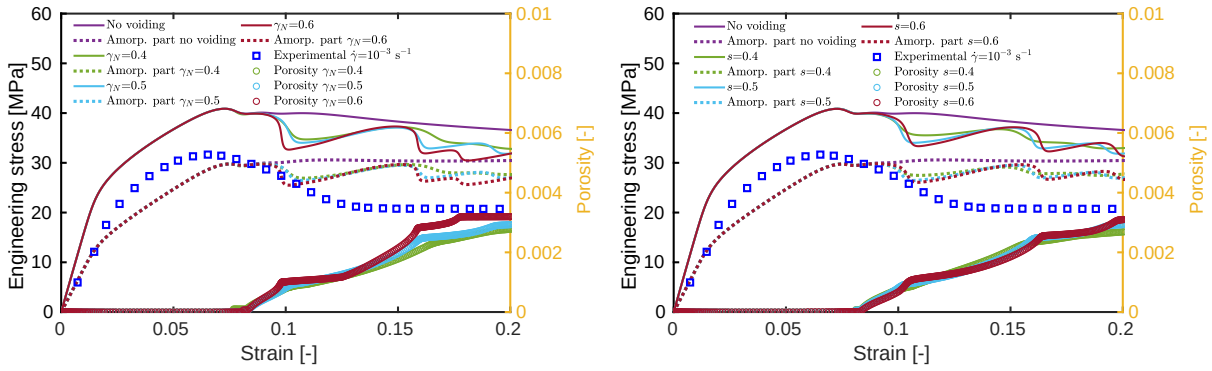

(a) *Influence of γ_N, s=0.5.* **(b)** *Influence of s, γ_N = 0.5.*

Figure 5.21: *The influence of the nucleation parameters on the void fraction, 23°C, strain-rate 10^{-3} s^{-1}.*

In this case, the void nucleation starts slightly after the maximum stress is reached. Following the description of nucleation, see Equation 4.31, this would mean that there is plastic deformation only after this point, as the nucleation is only present during plastic strain. Seeing that plastic deformation should start prior to yield this would have to be looked into. Additionally a non smooth stress-strain response after yielding is obtained. This also shows in the strain-rate of the slip systems and the amorphous phase. These results are shown in Figure 5.22a. The response shows more strain-rate peaks than the growth and standard model, while the profile between these outliers is smooth. In Figure 5.22b the other slip systems also start to activate simultaneously to the (010)[100] system and amorphous phase.

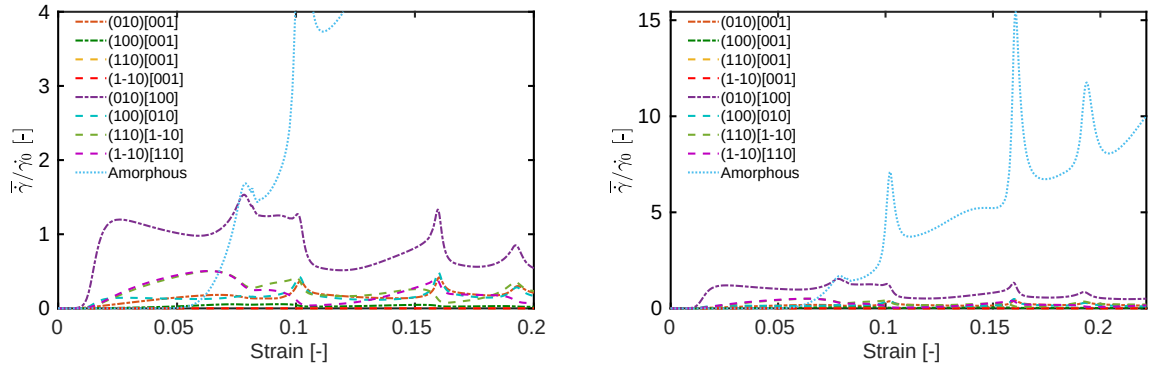

(a) *The complete normalised strain-rate response.* **(b)** *The zoomed in normalised strain-rate response.*

Figure 5.22: *The Composite Inclusion results for the nucleation model (γ_N=0.5, s=0.8).*

In Figures 5.23, 5.24 and 5.25 the polar plots are shown with the porosity, amorphous strain-rate and the strain-rate in slip system (010)[100]. Although the other slip systems show deformations, system (010)[100] remains the most active, therefore this systems strain-rate was used. Regarding the amorphous strain-rate and porosity they show similar patterns to the ones found previously, with growth and without growth.

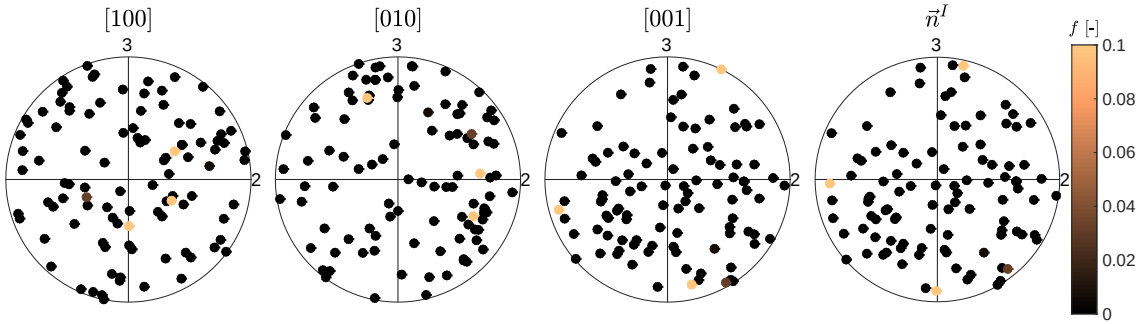

Figure 5.23: *Pole figures for the case including nucleation with from left to right: [100], [010], [001] and interface normal directions. The colour indicates the porosity in the amorphous phase.*

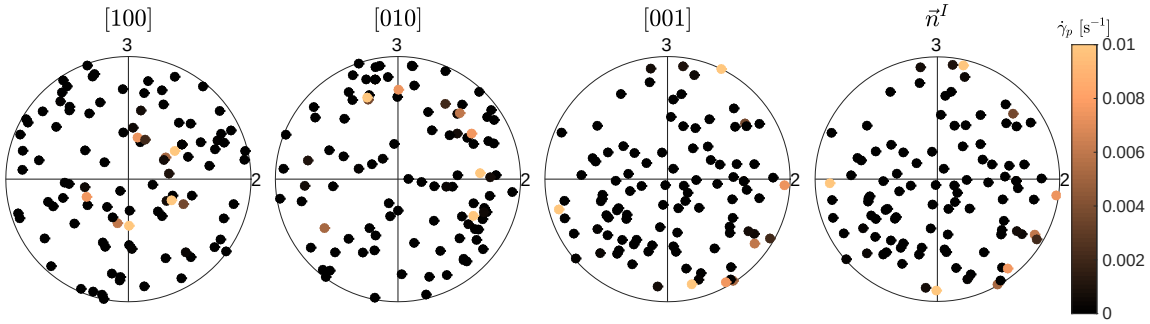

Figure 5.24: *Pole figures for the case including nucleation with from left to right: (100), (010), (001) and interface normal directions. The colour indicates the absolute strain-rate in the amorphous phase.*

Looking at the strain-rate over the slip system, only one inclusion shows large strain-rates. This is however

a different inclusion compared to the growth case, where also only one inclusion showed this large strain-rate. This difference could very well be caused by the strain-rate over the other slip systems, which did not show large influences without nucleation.

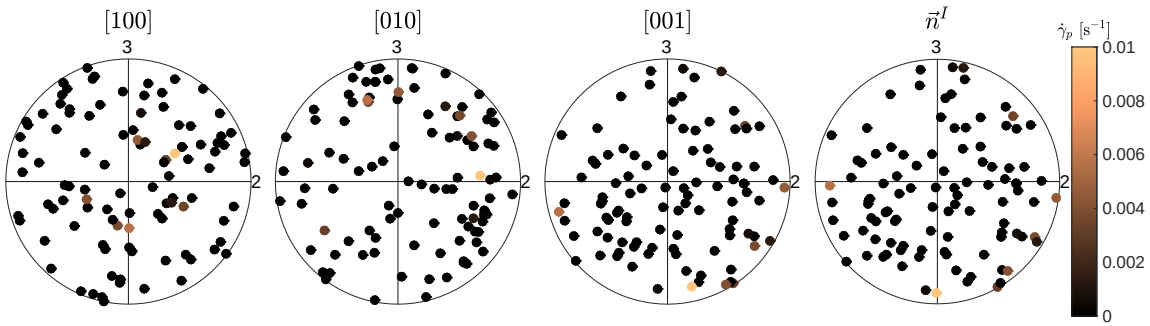

Figure 5.25: *Pole figures for the case including nucleation with from left to right: [100], [010], [001] and interface normal directions. The colour indicates the absolute shear-rate in the most active slipsystem (010)[100].*

In Figure 5.26 the results for the model including nucleation and growth are shown. These results show an even faster porosity growth, compared to just growth. This is due to added porosity of the nucleation. As the nucleation is based on the strain-rate, due to the large rate in one inclusion, the nucleation in this inclusion also increases.

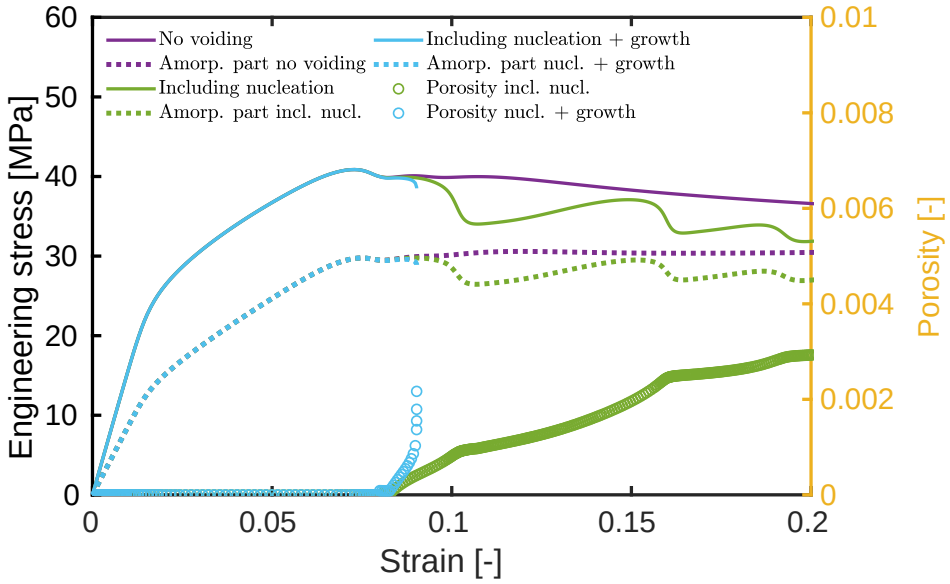

Figure 5.26: *The Composite Inclusion results for the nucleation model including and excluding growth, 23°C, strain-rate 10^{-3}, $\gamma_N = 0.5$, $s = 0.8$.*

5.2.4 The origin of the problem

To get a better understanding of the large strain-rates in a single inclusion, a better look at this inclusion is provided here. First the orientation of the inclusion is examined. This is done using the pole figure in Figure 5.18, 5.27 and 5.28.

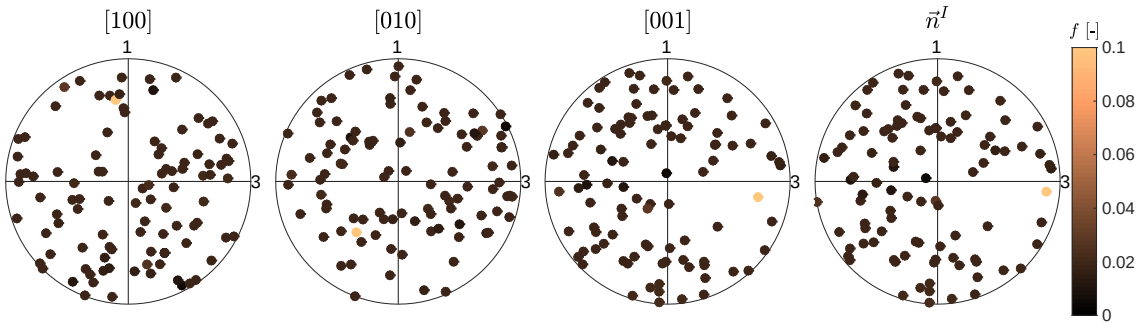

Figure 5.27: *Pole figures for the case including growth, starting porosity $f = 0.02$, with from left to right: [100], [010], [001] and interface normal directions, viewing direction 2. The colour indicates the porosity in the amorphous phase, .*

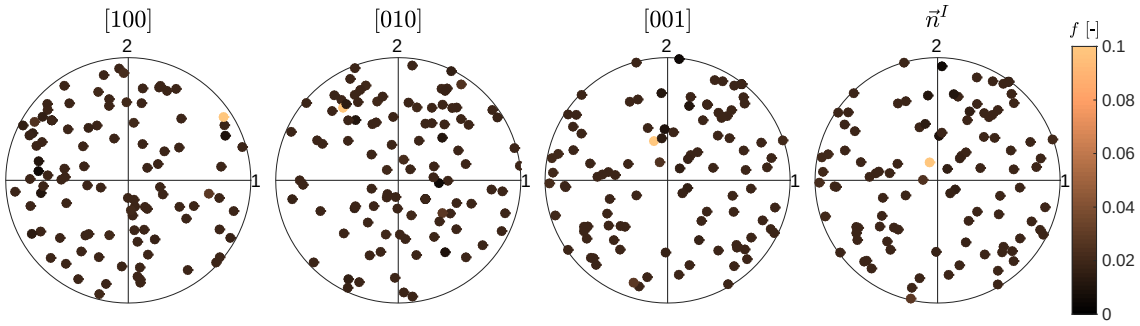

Figure 5.28: *Pole figures for the case including growth, starting porosity $f = 0.02$, with from left to right: [100], [010], [001] and interface normal directions, viewing direction 3. The colour indicates the porosity in the amorphous phase.*

These Figures show that the [100] direction, or the $\vec{a}$ direction in Figure 2.4, is oriented towards the tensile direction (1 direction). The normal of the interface is oriented in the 3 direction, nearly perpendicular to the tensile direction. The crystal direction, normally close to perpendicular to the interface, also shows a similar orientation as the interface normal. The orientation of the $\vec{a}$ direction is favourable for the most active slip system, (010)[100], as derived from Figure 5.17. To take a look at the interactions inside the inclusion, the strain-rates for the slip systems and amorphous phase for just this inclusion are shown in Figure 5.29. It can be seen that, when comparing the macroscopic strain rates of the growth case, Figure 5.17, the strain-rates in this inclusion are much higher. This single inclusion also shows the same peak in strain-rate at the same strain as the macroscopic result. Seeing that this inclusions strain-rate at this point is several times higher, this has a large effect on the macroscopic result. Looking at the stress shown in Figure 5.30, it can be seen that at the strain where the strain-rate increase occurs, the amorphous phase shifts from a negative stress in the 11 direction, to a positive. After a stress decrease in the crystalline phase occurs, the amorphous phase shows a very large hydrostatic stress increase and σ_{11} decrease. This indicated that the large void increase is driven by the crystalline phase.

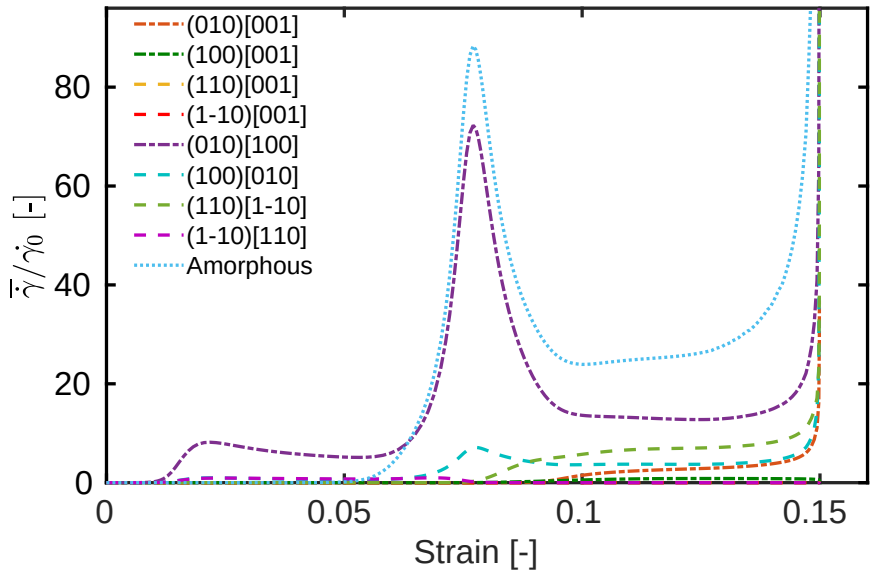

Figure 5.29: *The absolute normalised strain-rate for the 'problem' inclusion. 23°C, strain-rate 10^{-3} s^{-1}.*

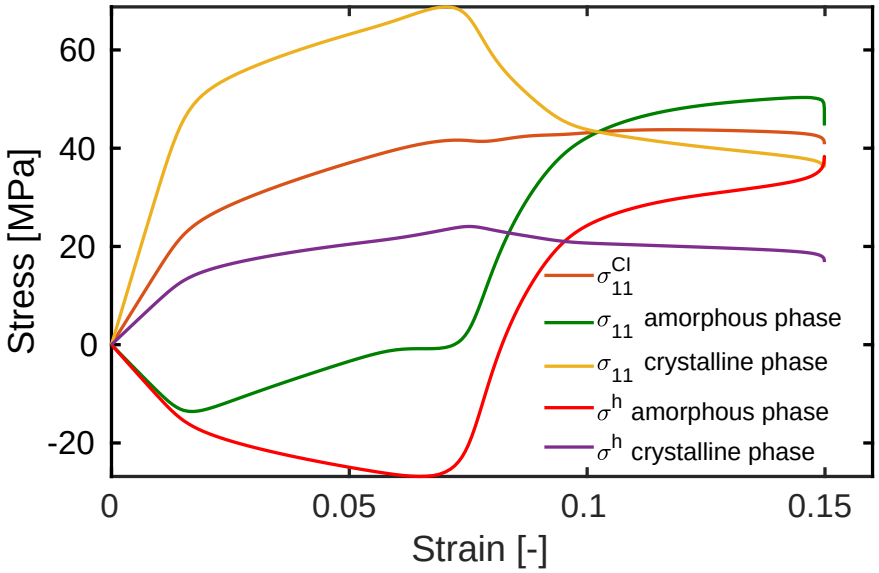

Figure 5.30: *The stress in the 'problem' inclusion over the strain. 23°C, strain-rate 10^{-3} s^{-1}.*

Looking at the orientations of the other inclusions, see Figures 5.19, 5.31 and 5.32, it can be seen that 'problem' inclusion interface normal is aligned close to the positive 3 direction. The other inclusions showing large deformations, also show alignment with their respective interface normals perpendicular to the loading axis. However, the 'problem' inclusion is the only inclusion aligned to this positive direction.

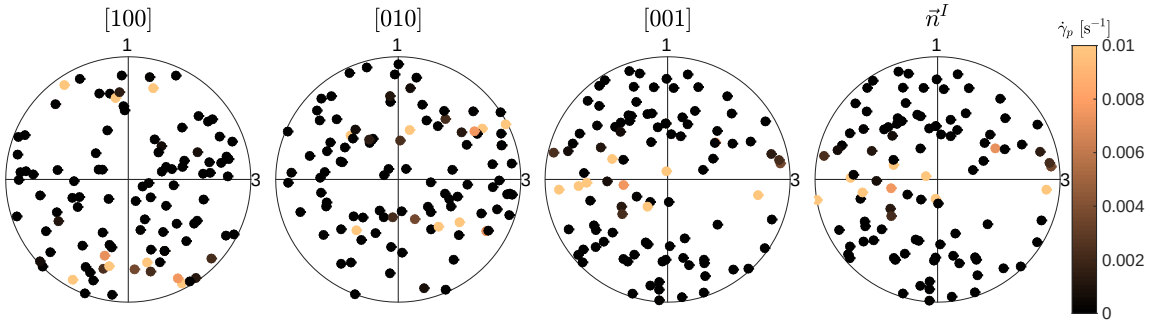

Figure 5.31: *Pole figures for the case including growth, starting porosity $f = 0.02$, with from left to right: [100], [010], [001] and interface normal directions, viewing direction 2. The colour indicates the porosity in the amorphous phase.*

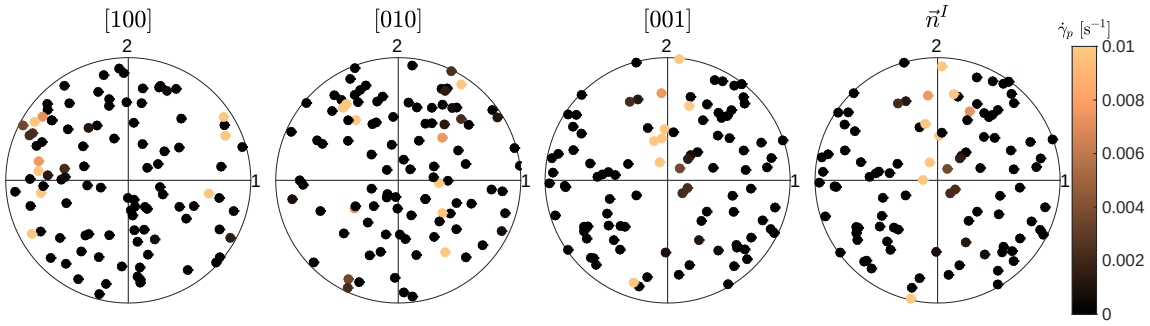

Figure 5.32: *Pole figures for the case including growth, starting porosity $f = 0.02$, with from left to right: [100], [010], [001] and interface normal directions, viewing direction 3. The colour indicates the strain-rate in the amorphous phase.*

6 Conclusion & Recommendations

For the improvement of the mechanical response of semi-crystalline polymers in tension a Gurson model was implemented in the existing Composite Inclusion model. To include this certain adjustments have been made to the EGP implementation. The model showed good results in the purely EGP model. In the EGP model the parameters of the Gurson model showed the expected results and no problems were encountered. The model can be tuned to show more or less voiding and the influence of voids and pressure can be changed to show a better stress-strain response.
However, while the implementation in the CIM was straightforward, as the EGP framework resembles the CIM, some problems were encountered. First of all, the way the CIM is described now does not support mulitple modes or mechanisms additional to voiding. To show a good response prior to yield multiple modes will be needed. Since the idea is to use one material model, in this case α-iPP, for a temperature range multiple mechanisms are required. This addition is currently not possible due to the fact that the pressure of the first mode is set as an overall pressure, whereas with the Gurson model, each mode requires an individual pressure.
Secondly, the α-iPP model itself shows some unexpected behaviour with large deformations concentrated in a few inclusions. While the model shows a macroscopically fitting result, this problem shows when incorporating voiding. The behaviour is dominated by these few inclusions, resulting in large void fractions and increased strain-rates of the inclusion. An attempt was made to resolve this problem, however as of yet unsuccessful. A proposition for this problem was given, by limiting the strain rate.
To compare the results of the CIM model to experimental results the data available from Caelers et al. [7] is not sufficient. This is due to the difference between the material point modelling of the CIM and the tensile experiments done by Caelers. While it should be possible to describe the correct macroscopic response in tension, by tuning the models parameters, the void fraction of the model might not resemble the actual porosity in a tensile test.
The first and most important recommendation would be to have a more gradual deformation pattern over the inclusions, as the domination of the macroscopic behaviour by very few inclusions leads to large void growths. While the best way to do this would be to find the reason for this unexpected behaviour, the faster and easier way would be to limit the strain-rate. This can be done as proposed in Section 5.2.2. This should limit the extreme cases and let most inclusions move freely.
The hydrostatic hardening component might also require more insight. The influence of this component is rather insignificant currently. This is probably due to the concentration of the deformation to certain inclusions. If this problem is resolved hydrostatic hardening might however still be needed to limit expansion of an inclusion.
Furthermore, a model supporting multiple modes and mechanisms should allow for a better response using a single parameter set. In the case of a single mode and mechanism model a parameter set is needed for every temperature and the mechanical response prior to yield is less accurate. In Section 3.2 a multi-mechanism description for the crystalline phase was given. This mechanism can also be used for the amorphous phase [24].
Lastly to get a good voiding response additional measurements are needed. While the trends of the readily available results from Caelers can be used, the actual void fraction and according stress can not be tuned accurately. A better result would be obtained by measuring the true stress and the void fraction. Furthermore the SAXS measurement done by Caelers showed no voiding for temperatures above 23°C for a 10^{-3} s^{-1} strain-rate, while differences in intensity hinted at voiding. Looking at other techniques to get clear image of voiding in iPP would be beneficial.

Bibliography

[1] B.J. Lee, D.M. Parks, S. Ahzi, "Micromechanical modeling of large plastic deformation and texture evolution in semi-crystalline polymers", Mech. Phys. Solids, Vol. 41, No. 10, pp. 1651-1687, 1993.

[2] J.A.W. van Dommelen, D.M. Parks, M.C. Boyce, W.A.M. Brekelmans, F.P.T. Baaijens, "Micromechanical modeling of intraspherulitic deformation of semi-crystalline polymers", Polymer, Vol. 44, pp. 6089-6101, 2003.

[3] M. Poluektov, J.A.W. van Dommelen, L.E. Goveart, I. Yakimets, M.G.D. Geers, "Micromechanical modelling of short-term and long-term large-strain behaviour of polyethylene terephthalate", Modelling Simul. Mater. Sci. Eng., Vol. 21, 2013.

[4] T.A. Tervoort, E.T. Klompen, L.E. Goveart, "A multi-mode approach to finite, three-dimensional, nonlinear viscoelastic behaviour of polymer glasses", Rheology, Vol. 40, pp. 779-797, 1996.

[5] N. Selles, N. Saintier, L. Laiarinandrasana, "Voiding mechanisms in semi-crystalline polyamide 6 during creep tests assessed by damage based constitutive relationships and finite elements calculations", Plasticity, Vol. 86, pp. 112-127, 2016.

[6] A. Pawlak, A. Galeski, "Plastic deformation of crystalline polymers: the role of cavitation and crystal plasticity", Macromolecules, Vol. 38, pp. 9688-9697, 2005.

[7] H.J.M. Caelers, "Structure tuning for enhanced properties in isotactic polypropylene", Eindhoven University of Technology, Eindhoven, 2017.

[8] A.L. Gurson, "Continuum theory of ductile rupture by void nucleation and growth: Part 1 - Yield criteria and flow rules for porouw ductile media", Engineering Materials and Technology, Vol. 76, pp. 2-15, 1977.

[9] A.L. Gurson, "Porous rigid-plastic materials containing rigid inclusions - yield function, plastic potential, and void nucleation", Fracture, Vol. 2, pp. 357-364, 1977.

[10] V. Tvergaard, A. Needleman, "Analysis of the cup-cone fracture in a round tensile bar", Acta metall., Vol. 32, No. 1, pp 157-169, 1984.

[11] V. Tvergaard, "Influence of voids on shear band instabilities under plane strain conditions", Fracture, Vol. 17, pp. 389-407, 1981.

[12] L. Morin, J.B. Leblond, D. Kondo, "A Gurson-type criterion for plastically anisotropic solids contain arbitrary ellipoisdal voids", Solids and Structures, Vol. 77, pp. 86-101, 2015.

[13] M. Gologanu, J.B. Leblond, "Approxiate models for ductile metals containing non-spherical voids - case of axisymmetric prolate ellipoisdal cavities", Mech. Phys. Solids, Vol. 41, No. 11, pp. 1723-1754, 1993.

[14] M. Gologanu, J.B. Leblond, J. Devaux, "Approxiate models for ductile metals containing non-spherical voids - case of axisymmetric oblate ellipoisdal cavities", Engineering Materials and Technology, Vol. 116, pp. 290-297, 1994.

[15] M. Gologanu, J.B. Leblond, G. Perrin, J. Devaux, "Recent extensions of Gurson's model for porous ductile materials", CISM courses and lectures, No. 377, pp. 61-130, 1997.

[16] A.A. Benzerga, J. Besson, A. Pineau, "Coalescence-controlled anisotropic ductile fracture", Engineering Materials and Technology, Vol. 121, pp. 221-229, 1999.

[17] J. Besson, C. Guillemer-Neel, "An extension of the Green and Gurson models to kinematic hardening", Mechanics of Materials, Vol. 35, pp. 1-18, 2003.

[18] Z.L. Zhang, C. Thaulow, J. Ødegård, "A complete Gurson model approach for ductile fracture", Engineering Fracture Mechanics, Vol. 67, pp. 155-168, 2000.

[19] S. Hao, W. Brocks, "The Gurson-Tvergaard-Needleman-model for rate and temperature-dependent materials with isotropic and kinematic hardening", Computational Mechanics, Vol. 20, pp. 34-40, 1997.

[20] K. Madou, J.B. Leblond, "A Gurson-type criterion for porous ductile solids containing arbitrary ellipsoidal voids - II: Determination of yield criterion parameters", Mech. Phys. Solids, Vol. 60, No. 5, pp. 1039-1058, 2012.

[21] J. Besson, "Continuum models of ductile fracture: A review", Damage Mechanics, Vol. 19, pp. 3-52, 2010.

[22] A. Needleman, J.R. Rice, "Limits of ductility set by plastic flow localization", Mechanics of sheet metal forming, pp. 237-267, 1978.

[23] C.C. Chu, A. Needleman, "Void nucleation effects in biaxially stretched sheets", Materials and Technology, Vol. 102, pp. 249-256, 1980.

[24] A. Sedighiamiri, L.E. Govaert, J.A.W. van Dommelen, "Micromechanical modeling of the deformation kinetic of semicrystalline polymers", Polymer Physics, Vol. 49, pp. 1297-1310, 2011.

[25] M. van Drongelen, T.B. van Erp, G.W.M. Peters, "Quantification on non-isothermal multi-phase crystallization of isotactic polypropylene: the influence of cooling rate and pressure", Polymer, Vol. 53, pp. 4758-4769, 2012.

[26] L. Lin, A.S. Argon, "Structure and plastic deformation of polyethylene", Mater. Sci., Vol. 29, pp. 294-323, 1994.

[27] R.M. Gohil, "Morphology-property relationship in oriented PET films: microstructural reorganization during heat treatment", Applied Polymer Science, Vol. 52, pp. 925-944, 1994.

[28] P.J. Barham, A. Keller, "High-strength polyethylene fibres from solution and gel spinning", Materials Science, Vol. 20, pp. 2281-2302, 1985.

[29] T.B. van Erp, "Structure development and mechanical performance of polypropylene", Eindhoven University of Technology, Eindhoven, 2012.

[30] P.B. Bowden, R.J. Young, "Deformation mechanisms in crystalline polymers", Material science, Vol. 9, pp. 2034-2051, 1974.

[31] S. Ahzi, B.J. Lee, R.J. Asaro, "Plasticity and anisotropy evolution in crystalline polymers", Mater. Sci. Eng., Vol. 189, pp. 35-44, 1994.

[32] B. Chang, K. Schneider, F. Xiang, R. Vogle, S. Roth, G. Heidrich, "Critical strains for lamellae deformation and cavitation during uniaxial stretching of annealed isotactit polypopylene", Macromolecules, Vol. 51, pp. 6276-6290, 2018.

[33] F. Chu, T. Yamaoka, H. Ide, Y. Kimura, "Microoid formation process during plastic deformation of β-form polypropylene", Polymer, Vol. 35, pp. 3442-3448, 1994.

[34] J.A.W. van Dommelen, Lecture notes, Topic: ”Computational and experimental micromechanics”, 4MM20, Eindhoven University of Technology, Eindhoven, 2015.

[35] S. Humbert, O. Lame, J.M. Chenal, C. Rochas, G. Vigier, ”New insight on initiation of cavitation in Semicrystalline polymers: In-Situ SAXS measurements”, Macromolecules, Vol. 43, pp. 7212-7221, 2010.

[36] H. Zhang, A.K. Scholz, J. Crevoisier, F. Vion-Loisel, G. Besnard, A. Hexemer, H.R. Brown, E.J. Kramer, C. Creton, ”Nanocavitation in carbon black filled styrene-butadiene rubber under tension detected by real time small angle x-ray scattering”, Marcomolecules, Vol. 45, pp. 1529-1543, 2012.

[37] D. Lyu, R. Chen, Y. Lu, Y. Men, ”Subsequent but independent cavitation processes in isotactic polypropylene during stretching at small- and large-strain regimes”, Ind. Eng. Chem. Res., Vol. 57, 8927-8937, 2018.

[38] A. Galeski, ”Strength and toughness of crystalline polymer systems”, Prog. Polym. Sci., Vol. 28, pp. 1643-1699, 2003.

[39] A. Pawlak, A. Galeski, ”Cavitation during tensile deformation of polypropylene”, Macromolecules, Vol. 41, pp. 2839-2851, 2008.

[40] N. Selles, P. Cloetens, H. Prooudhon, T.F. Morgeneyer, O. Klinkova, N. Saintier, L. Laiarinandrasana, Macromolecules, Vol. 50, pp. 4372-4783, 2017.

[41] L.E. Govaert, P.H.M. Timmermans, W.A.M. Brekelmans, ”The influence of intrinsic strain softening on strain localization in polycarbonate: modeling and experimental validation”, Engineering Materials and Technology, Vol. 122, pp. 177-185, 2000.

[42] E.T.J. Klompen, ”Mechanical properties of solid polymers: constitutive modelling of long and short term behaviour”, Eindhoven University of Technology, Eindhoven, 2005.

[43] L.C.A. van Breemen, E.T.J. Klompen, L.E. Govaert, H.E.H. Meijer, ”Extending the EGP constitutive model for polymer glasses to multiple relaxation times”, Mech. Phy. Solids, Vol. 59, pp. 2191-2207, 2011.

[44] L.C.A. van Breemen, T.A.P. Engels, E.T.J. Klompen, D.J.A. Senden, L.E. Govaert, ”Rate- and temperature-dependent strain softening in solid polymers”, Polymer Physics, Vol. 50, pp. 1757-1771, 2012.

[45] T. Ree, H. Eyring, ”Theory of non-newtonian flow I. Solid plastic system”, Applied Physics, Vol. 26, pp. 793-800, 1955.

[46] M. Mirkhalaf, J.A.W. van Dommelen, L.E. Govaert, J. Furmanski, M.G.D. Geers, ”Micromechanical modeling of anisotropic behavior of oriented semicrystalline polymers”, Polymer Physics, Vol. 57, pp. 378-391, 2019.

[47] A.C. Steenbrink, E. van der Giessen, P.D. Wu, ”Void growth in glassy polymers”, Mech. Phys. Solids, Vol. 45, No. 3, pp. 405-437, 1997.

[48] K. Tashiro, M. Kobayashi, H. Tadokoro, ”Vibrational spectra and theoretical three-dimensional elastic constants of isotactic polypropylene crystal: an important role of anharmonic vibrations”, Polymer, Vol. 24, pp. 899-916, 1992.

[49] K.B. Petersen, M.S. Pedersen, ”The Matrix Cookbook”, 2012.

[50] S.M. Selby, ”Standard Mathematical Tables”, CRC Press, 1974.

Appendices

A Gurson model derivation

Here the derivations for the tangents of the EGP model including the Gurson model are described. Since the derivation of Equation 4.14 is straightforward, this will not be discussed. The next derivative, $\frac{\partial \Phi}{\partial \bar{\boldsymbol{\sigma}}}$ is a little less straightforward. Given the potential as:

$$\Phi = \frac{1}{2}\frac{\bar{\boldsymbol{\sigma}}^d : \bar{\boldsymbol{\sigma}}^d}{\tau^2} + 2f\cosh(\frac{\sqrt{3}}{2}\frac{\frac{1}{3}tr(\bar{\boldsymbol{\sigma}})}{\tau}) - (1+f^2) = 0, \tag{A.1}$$

the partial derivative with respect to the driving stress $\bar{\boldsymbol{\sigma}}$ has to be calculated. This can be done by first rewriting the potential given that $\mathbf{A} : \mathbf{B} = tr(\mathbf{A}\cdot\mathbf{B})$ and $\mathbf{A}\cdot\mathbf{A} = \mathbf{A}^2$, leading to the following expression:

$$\frac{\partial \Phi}{\partial \bar{\boldsymbol{\sigma}}} = \frac{1}{2\tau^2}\frac{\partial}{\partial \bar{\boldsymbol{\sigma}}}tr(\bar{\boldsymbol{\sigma}}^{d^2}) + \frac{\partial}{\partial \bar{\boldsymbol{\sigma}}}(2f\cosh(\frac{\sqrt{3}}{2}\frac{\frac{1}{3}tr(\bar{\boldsymbol{\sigma}})}{\tau})). \tag{A.2}$$

$\bar{\boldsymbol{\sigma}}^d$ and $\bar{\boldsymbol{\sigma}}^h$ can both be rewritten:

$$\bar{\boldsymbol{\sigma}}^d = \bar{\boldsymbol{\sigma}} - \frac{1}{3}tr(\bar{\boldsymbol{\sigma}})\mathbf{I}, \tag{A.3}$$

$$\bar{\boldsymbol{\sigma}}^h = \frac{1}{3}tr(\bar{\boldsymbol{\sigma}})\mathbf{I}. \tag{A.4}$$

This results in the following expression for $\frac{\partial \Phi}{\partial \bar{\boldsymbol{\sigma}}}$:

$$\frac{\partial \Phi}{\partial \bar{\boldsymbol{\sigma}}} = \frac{1}{2\tau^2}\frac{\partial}{\partial \bar{\boldsymbol{\sigma}}}tr\left[\left(\bar{\boldsymbol{\sigma}} - \frac{1}{3}tr(\bar{\boldsymbol{\sigma}})\mathbf{I}\right)^2\right] + \frac{\partial}{\partial \bar{\boldsymbol{\sigma}}}\left(2f\cosh(\frac{\sqrt{3}}{2}\frac{\frac{1}{3}tr(\bar{\boldsymbol{\sigma}})}{\tau})\right). \tag{A.5}$$

$$\frac{\partial \Phi}{\partial \bar{\boldsymbol{\sigma}}} = \frac{1}{2\tau^2}\frac{\partial}{\partial \bar{\boldsymbol{\sigma}}}tr\left[\bar{\boldsymbol{\sigma}}^2 - \frac{2}{3}tr(\bar{\boldsymbol{\sigma}})\cdot\bar{\boldsymbol{\sigma}} + \frac{1}{9}tr(\bar{\boldsymbol{\sigma}})^2\cdot\mathbf{I}\right] + \frac{\partial}{\partial \bar{\boldsymbol{\sigma}}}\left(2f\cosh(\frac{\sqrt{3}}{2}\frac{\frac{1}{3}tr(\bar{\boldsymbol{\sigma}})}{\tau})\right). \tag{A.6}$$

$$\frac{\partial \Phi}{\partial \bar{\boldsymbol{\sigma}}} = \frac{1}{2\tau^2}\frac{\partial}{\partial \bar{\boldsymbol{\sigma}}}\left[tr(\bar{\boldsymbol{\sigma}}^2) - \frac{2}{3}tr(tr(\bar{\boldsymbol{\sigma}})\cdot\bar{\boldsymbol{\sigma}}) + \frac{1}{9}tr(tr(\bar{\boldsymbol{\sigma}})^2\cdot\mathbf{I})\right] + \frac{\partial}{\partial \bar{\boldsymbol{\sigma}}}\left(2f\cosh(\frac{\sqrt{3}}{2}\frac{\frac{1}{3}tr(\bar{\boldsymbol{\sigma}})}{\tau})\right). \tag{A.7}$$

Using the fact that $tr(tr(\mathbf{X})\cdot\mathbf{Y}) = tr(\mathbf{X})\cdot tr(\mathbf{Y})$, with X and Y being two tensors, $tr(tr(\bar{\boldsymbol{\sigma}})\cdot\bar{\boldsymbol{\sigma}})$ can be written as $tr(\bar{\boldsymbol{\sigma}})^2$. With the trace of the identity tensor being 3 the following expression can be found:

$$\frac{\partial \Phi}{\partial \bar{\boldsymbol{\sigma}}} = \frac{1}{2\tau^2}\frac{\partial}{\partial \bar{\boldsymbol{\sigma}}}\left[tr(\bar{\boldsymbol{\sigma}}^2) - \frac{2}{3}tr(\bar{\boldsymbol{\sigma}})^2 + \frac{3}{9}tr(\bar{\boldsymbol{\sigma}})^2\right] + \frac{\partial}{\partial \bar{\boldsymbol{\sigma}}}\left(2f\cosh(\frac{\sqrt{3}}{2}\frac{\frac{1}{3}tr(\bar{\boldsymbol{\sigma}})}{\tau})\right). \tag{A.8}$$

The following rules for derivatives of traces are needed [49]:

$$\frac{\partial}{\partial \mathbf{X}}tr(\mathbf{X})^2 = 2tr(\mathbf{X})\mathbf{I}, \tag{A.9}$$

$$\frac{\partial}{\partial \mathbf{X}}tr(\mathbf{F}(\mathbf{X})) = \mathbf{F}'(\mathbf{X})^T. \tag{A.10}$$

With $\bar{\boldsymbol{\sigma}}$ being symmetric, applying these rules to equation A.8 leads to the following result:

$$\frac{\partial \Phi}{\partial \bar{\boldsymbol{\sigma}}} = \frac{1}{2\tau^2}\left[2\bar{\boldsymbol{\sigma}} - \frac{4}{3}tr(\bar{\boldsymbol{\sigma}})\mathbf{I} + \frac{2}{3}tr(\bar{\boldsymbol{\sigma}})\mathbf{I}\right] + \left(\frac{f}{\sqrt{3}\tau}\mathbf{I}\sinh(\frac{\sqrt{3}}{2}\frac{\frac{1}{3}tr(\bar{\boldsymbol{\sigma}})}{\tau})\right). \tag{A.11}$$

Rewriting $(2\bar{\boldsymbol{\sigma}} - \frac{4}{3}tr(\bar{\boldsymbol{\sigma}})\mathbf{I} + \frac{2}{3}tr(\bar{\boldsymbol{\sigma}})\mathbf{I})$ utilizing A.3 to leads to:

$$\frac{\partial \Phi}{\partial \bar{\boldsymbol{\sigma}}} = \frac{\bar{\boldsymbol{\sigma}}^d}{\tau^2} + \frac{f}{\sqrt{(3)}\tau}\mathbf{I}\sinh(\frac{\sqrt{3}}{2}\frac{\frac{1}{3}tr(\bar{\boldsymbol{\sigma}})}{\tau}). \tag{A.12}$$

The next derivative that needs some clarification is the partial derivative of the plastic deformation rate with respect to the driving stress, see Equation 4.18. This partial derivative can be written as follows:

$$\frac{\partial D_p}{\partial \bar{\boldsymbol{\sigma}}} = (1-f)\dot{\gamma}^p\tau\frac{\partial}{\partial \bar{\boldsymbol{\sigma}}}\left[(\bar{\boldsymbol{\sigma}} : \frac{\partial \Phi}{\partial \bar{\boldsymbol{\sigma}}})^{-1}\frac{\partial \Phi}{\partial \bar{\boldsymbol{\sigma}}}\right]. \tag{A.13}$$

$$\frac{\partial D_p}{\partial \bar{\boldsymbol{\sigma}}} = (1-f)\dot{\gamma}^p\tau\left[\frac{\partial}{\partial \bar{\boldsymbol{\sigma}}}\left((\bar{\boldsymbol{\sigma}} : \frac{\partial \Phi}{\partial \bar{\boldsymbol{\sigma}}})^{-1}\right)\frac{\partial \Phi}{\partial \bar{\boldsymbol{\sigma}}} + (\bar{\boldsymbol{\sigma}} : \frac{\partial \Phi}{\partial \bar{\boldsymbol{\sigma}}})^{-1}\frac{\partial^2 \Phi}{\partial \bar{\boldsymbol{\sigma}}^2}\right]. \tag{A.14}$$

For ease of calculation the derivative can be split in 2 parts, as shown in A.14. Using the relation [50],

$$\frac{\partial(\mathbf{X}^{-1})}{\partial \mathbf{Y}} = -\mathbf{X}^{-1}\cdot\frac{\partial \mathbf{X}}{\partial \mathbf{Y}}\cdot\mathbf{X}^{-1}, \tag{A.15}$$

the derivative can be derived as follows:

$$\frac{\partial}{\partial \bar{\boldsymbol{\sigma}}}((\bar{\boldsymbol{\sigma}} : \frac{\partial \Phi}{\partial \bar{\boldsymbol{\sigma}}})^{-1}) = -(\bar{\boldsymbol{\sigma}} : \frac{\partial \Phi}{\partial \bar{\boldsymbol{\sigma}}})^{-1}\cdot\frac{\partial(\bar{\boldsymbol{\sigma}} : \frac{\partial \Phi}{\partial \bar{\boldsymbol{\sigma}}})}{\partial \bar{\boldsymbol{\sigma}}}\cdot(\bar{\boldsymbol{\sigma}} : \frac{\partial \Phi}{\partial \bar{\boldsymbol{\sigma}}})^{-1}. \tag{A.16}$$

This leads to the following:

$$\frac{\partial}{\partial \bar{\boldsymbol{\sigma}}}((\bar{\boldsymbol{\sigma}} : \frac{\partial \Phi}{\partial \bar{\boldsymbol{\sigma}}})^{-1}) = -(\bar{\boldsymbol{\sigma}} : \frac{\partial \Phi}{\partial \bar{\boldsymbol{\sigma}}})^{-1}\cdot({}^4\mathbf{I} : \frac{\partial \Phi}{\partial \bar{\boldsymbol{\sigma}}} + \bar{\boldsymbol{\sigma}} : \frac{\partial^2 \Phi}{\partial \bar{\boldsymbol{\sigma}}^2})\cdot(\bar{\boldsymbol{\sigma}} : \frac{\partial \Phi}{\partial \bar{\boldsymbol{\sigma}}})^{-1}, \tag{A.17}$$

Combining the parts as described in Equation A.14 leads to:

$$\frac{\partial \mathbf{D}_p}{\partial \bar{\boldsymbol{\sigma}}} = (1-f)\dot{\gamma}_p\tau\left[\frac{\partial \Phi}{\partial \bar{\boldsymbol{\sigma}}}\otimes\left(-(\bar{\boldsymbol{\sigma}} : \frac{\partial \Phi}{\partial \bar{\boldsymbol{\sigma}}})^{-1}({}^4\mathbf{I} : \frac{\partial \Phi}{\partial \bar{\boldsymbol{\sigma}}} + \bar{\boldsymbol{\sigma}} : \frac{\partial^2 \Phi}{\partial \bar{\boldsymbol{\sigma}}^2})(\bar{\boldsymbol{\sigma}} : \frac{\partial \Phi}{\partial \bar{\boldsymbol{\sigma}}})^{-1}\right) + (\bar{\boldsymbol{\sigma}} : \frac{\partial \Phi}{\partial \bar{\boldsymbol{\sigma}}})^{-1}\frac{\partial^2 \Phi}{\partial \bar{\boldsymbol{\sigma}}^2}\right]. \tag{A.18}$$

This derivative leads to another derivative, $\frac{\partial^2 \Phi}{\partial \bar{\boldsymbol{\sigma}}^2}$. With $\frac{\partial \Phi}{\partial \bar{\boldsymbol{\sigma}}}$ defined in A.12 the following expression is obtained:

$$\frac{\partial^2 \Phi}{\partial \bar{\boldsymbol{\sigma}}^2} = \frac{1}{\tau^2}(\frac{\partial \bar{\boldsymbol{\sigma}}^T}{\partial \bar{\boldsymbol{\sigma}}} - \frac{1}{3}\frac{\partial}{\partial \bar{\boldsymbol{\sigma}}}(tr(\bar{\boldsymbol{\sigma}})\mathbf{I}) + \frac{f}{\sqrt{3}\tau}\frac{\partial}{\partial \bar{\boldsymbol{\sigma}}}\mathbf{I}\sinh(\frac{\sqrt{3}}{2}\frac{\frac{1}{3}tr(\bar{\boldsymbol{\sigma}})}{\tau}). \tag{A.19}$$

The derivative of $\frac{\partial \bar{\boldsymbol{\sigma}}}{\partial \bar{\boldsymbol{\sigma}}}$ can be given here as a fourth order identity tensor:

$${}^4\mathbf{I} = e_i\otimes e_j\otimes e_j\otimes e_i, \tag{A.20}$$

The derivative of $\frac{\partial}{\partial \bar{\boldsymbol{\sigma}}}(tr(\bar{\boldsymbol{\sigma}})\mathbf{I})$ is given as:

$$\frac{\partial}{\partial \bar{\boldsymbol{\sigma}}}(tr(\bar{\boldsymbol{\sigma}})\mathbf{I}) = e_i \otimes e_i \otimes e_j \otimes e_j, \tag{A.21}$$

for convenience given as ${}^4\mathbf{I}^*$. Combining this then into Equation A.19 leads to:

$$\frac{\partial^2 \Phi}{\partial \bar{\boldsymbol{\sigma}}^2} = \frac{1}{\tau^2}({}^4\mathbf{I} - \frac{1}{3\tau}{}^4\mathbf{I}^*) + \frac{f}{6\tau^2}{}^4\mathbf{I}^* \cosh(\frac{\sqrt{3}}{2}\frac{\frac{1}{3}tr(\bar{\boldsymbol{\sigma}})}{\tau}). \tag{A.22}$$